Monthly Notices
of the
ROYAL ASTRONOMICAL SOCIETY

MNRAS **493,** 1–28 (2020)
Advance Access publication 2020 January 17

doi:10.1093/mnras/staa135

The impact of wind scalings on stellar growth and the baryon cycle in cosmological simulations

Shuiyao Huang [1]★ Neal Katz,[1] Romeel Davé [2,3,4] Benjamin D. Oppenheimer,[5] David H. Weinberg,[6] Mark Fardal,[1,7] Juna A. Kollmeier [8] and Molly S. Peeples [7,9]

[1]*Astronomy Department, University of Massachusetts, Amherst, MA 01003, USA*
[2]*Institute for Astronomy, Royal Observatory, University of Edinburgh, Edinburgh EH9 3HJ, UK*
[3]*University of the Western Cape, Bellville, Cape Town 7535, South Africa*
[4]*South African Astronomical Observatories, Observatory, Cape Town 7925, South Africa*
[5]*CASA, Department of Astrophysical and Planetary Sciences, University of Colorado, Boulder, CO 80309, USA*
[6]*Astronomy Department and CCAPP, Ohio State University, Columbus, OH 43210, USA*
[7]*Space Telescope Science Institute, Baltimore, MD 21218, USA*
[8]*Observatories of the Carnegie Institution of Washington, 813 Santa Barbara Street, Pasadena, CA 91101, USA*
[9]*Department of Physics and Astronomy, Johns Hopkins University, 3400 N. Charles Street, Baltimore, MD 21218, USA*

Accepted 2019 December 24. Received 2019 December 9; in original form 2019 October 17

ABSTRACT

Many phenomenologically successful cosmological simulations employ kinetic winds to model galactic outflows. Yet systematic studies of how variations in kinetic wind scalings might alter observable galaxy properties are rare. Here we employ GADGET-3 simulations to study how the baryon cycle, stellar mass function, and other galaxy and CGM predictions vary as a function of the assumed outflow speed and the scaling of the mass-loading factor with velocity dispersion. We design our fiducial model to reproduce the measured wind properties at 25 per cent of the virial radius from the Feedback In Realistic Environments simulations. We find that a strong dependence of $\eta \sim \sigma^5$ in low-mass haloes with $\sigma < 106\,\mathrm{km\,s^{-1}}$ is required to match the faint end of the stellar mass functions at $z > 1$. In addition, faster winds significantly reduce wind recycling and heat more halo gas. Both effects result in less stellar mass growth in massive haloes and impact high ionization absorption in halo gas. We cannot simultaneously match the stellar content at $z = 2$ and 0 within a single model, suggesting that an additional feedback source such as active galactic nucleus might be required in massive galaxies at lower redshifts, but the amount needed depends strongly on assumptions regarding the outflow properties. We run a $50\,\mathrm{Mpc}\,h^{-1}$, 2×576^3 simulation with our fiducial parameters and show that it matches a range of star-forming galaxy properties at $z \sim 0$–2.

Key words: methods: numerical – galaxies: evolution – galaxies: general.

1 INTRODUCTION

Galactic scale outflows (galactic winds) driven by star formation processes have been recognized as a critical ingredient in galaxy evolution. Galactic winds are observed ubiquitously among star-forming galaxies in both the local and distant Universe, and their properties are often found to correlate with the properties of the central galaxy such as the star formation rate (SFR) and the circular velocity (Martin 2005; Rupke, Veilleux & Sanders 2005; Heckman & Borthakur 2016). The short-lived, massive stars formed in star-forming galaxies release a considerable amount of energy and momentum during their short lifetimes through radiation, stellar winds, and supernova (SN) explosions. Collectively, these effects could efficiently drive the large-scale outflow of dense, metal-enriched gas from the interstellar medium (ISM) to large distances from the galaxy, making a strong impact on galaxy growth and also on the properties of the circumgalactic medium (CGM). Galactic winds have been implemented as a subgrid model in cosmological simulations, in which they play a critical role in explaining the suppressed star formation in dwarf galaxies and the metal content in the CGM (e.g. Oppenheimer & Davé 2008; Oppenheimer et al. 2012; Ford et al. 2013).

However, implementing galactic winds in cosmological simulations remains a challenge because of our limited knowledge of the wind driving mechanism, and the limited resolution of large-volume simulations. Self-consistently generating galactic winds by

★ E-mail: shuiyao@astro.umass.edu

explicitly modelling the key wind driving mechanisms is still a challenging problem that is under active study (Zhang 2018). More importantly, the physical processes that are critical to driving winds occur on scales that are so small that they remain unresolvable in even the highest resolution zoom-in simulations of today (e.g. Scannapieco & Brüggen 2015; Schneider & Robertson 2017; Hopkins et al. 2018). As a consequence, modern cosmological simulations adopt a variety of subgrid prescriptions that describe how to launch galactic winds from simulated galaxies (Springel & Hernquist 2003; Oppenheimer & Davé 2006; Stinson et al. 2006; Agertz et al. 2013; Schaye et al. 2015; Hopkins et al. 2018; Pillepich et al. 2018a). This diversity of numerical recipes for galactic winds leads to many different predictions from these simulations (Scannapieco et al. 2012; Sadoun et al. 2016; Sembolini et al. 2016b; Valentini et al. 2017).

The *kinetic feedback* models (Springel & Hernquist 2003; Oppenheimer & Davé 2006), like those that we employ, rely on scaling relations that connect the macroscopic properties of galactic winds, such as the wind velocity $v_{\rm w}$ and the mass-loading factor η, defined as the ratio between the outflow rate ($\dot{M}_{\rm w}$) and the SFR to the resolved properties of their host galaxies such as the halo mass $M_{\rm h}$, or some characteristic velocity (e.g. the velocity dispersion σ). Though the properties of galactic winds and the physical mechanisms that generate them are still poorly understood, there have been many constraints on these scaling relations from observations, analytic calculations, and simulations (Murray, Quataert & Thompson 2005; Rupke et al. 2005; Murray, Ménard & Thompson 2011).

The fiducial wind prescription that we have used in many of our previous papers (e.g. Oppenheimer & Davé 2006; Davé et al. 2013; Ford et al. 2016) was motivated by the analytic momentum-driven and energy-driven wind models developed by Murray et al. (2005). In the momentum-driven scenario, the outflow is driven in a momentum-conserving manner by the radiation pressure from massive stars and SNe acting on the dust particles that is coupled to the cool gas. The momentum flux overwhelms the gravitational potential of the dark matter halo in early phases and accelerates the cool gas from within the star-forming region to an asymptotic velocity at the virial radius of the dark matter halo. Assuming an isothermal potential and ignoring hydrodynamic forces, Murray et al. (2005) derived the evolution of the wind speed as a function of radius as

$$v_{\rm w}(r) = 2\sigma_{\rm 1D}\sqrt{(f_{\rm L}-1)\ln\left(\frac{r}{R_0}\right)}, \quad (1)$$

where $\sigma_{\rm 1D}$ is the one-dimensional velocity dispersion measured for an isothermal sphere, $f_{\rm L} = L/L_{\rm M}$ is the ratio between the luminosity of the galaxy and the critical Eddington luminosity, and R_0 is the radius from which the wind is launched. They also derived the scalings between η and σ as $\eta \propto \sigma^{-1}$ based on the conservation of momentum. In our more recent simulations, we actually assume that $\eta \propto \sigma^{-2}$ for small galaxies, which is the scaling one would expect for energy-driven winds by an SN.

Even if this is not the correct physics behind real galactic winds, this modified momentum-driven model predicts scaling relations between global quantities such as mass loading, wind velocity, and the stellar mass that, when included in cosmological hydrodynamic simulations, are broadly consistent with many observational constraints (Oppenheimer & Davé 2006, 2008; Davé et al. 2010; Oppenheimer et al. 2010; Davé, Finlator & Oppenheimer 2011b; Davé, Oppenheimer & Finlator 2011a; Davé et al. 2013; Ford et al. 2016). However, implementing the wind model into our simulations is more complicated than suggested by the above equations. Instead of launching a wind from any radius R_0 as in equation (1), we eject wind particles with an initial velocity $v_{\rm w}$ from star-forming regions that inhabit the centre of the galactic potential and let them propagate out under the combined gravitational and hydrodynamical forces (we ignore hydrodynamic interactions for a short period after wind launch; see below for details). Furthermore, the dynamical evolution of wind particles in our simulation is very different from the analytical solution of Murray et al. (2005) for several reasons. First, the gravitational potentials in our simulated haloes are steeper than the isothermal sphere assumed in Murray et al. (2005), especially in the central region where baryonic matter dominates. Secondly, our simulations do not explicitly include radiation pressure, which in their calculation accelerates the outflow all the way out to the virial radius. Thirdly, wind particles in our simulation are further slowed down by hydrodynamic interactions with the gas in the CGM or the intergalactic medium (IGM). Finally, these interactions are probably not accurately evolved owing to resolution and other numerical issues.

Recent zoom-in simulations of individual galaxies provide further insights into the scaling relations between the launched winds and their host galaxies (Muratov et al. 2015; Christensen et al. 2016). Capable of resolving GMC scales and the turbulent nature of the ISM, these simulations drive winds by explicitly modelling physical processes that depend on the local ISM properties and analyse how the wind behaviours depend on the global properties of their host galaxies, therefore better bridging the gap between the governing physics on small scales and the impact of the winds in the broader context of galaxy formation [but still not resolving all the scales critical for driving winds (e.g. Schneider & Robertson 2017)].

Using a series of simulations that span four decades in halo mass up to $10^{12}\,{\rm M}_\odot$ and covering a redshift range from $z = 0$ to 4, the Feedback In Realistic Environments (FIRE) project (Muratov et al. 2015, hereafter M15) derives how mass-loading factors and wind speeds depend on the circular velocity, the halo mass, and the stellar mass of the host galaxies. They report faster wind speeds in massive haloes than in our previous simulations using the fiducial wind model described above (and in more detail below). They also report a stronger scaling between the mass-loading factor and the circular velocity with $\eta \propto v_{\rm c}^{-3.3}$, steeper than the energy-driven wind scaling, $\eta \propto v_{\rm c}^{-2}$, which we assume in our simulations for low-mass galaxies. Christensen et al. (2016) simulate and analyse over 20 spiral and dwarf galaxies covering halo masses from $10^{9.5}$ to $10^{12}\,{\rm M}_\odot$. Despite using a very different feedback model, they obtain a similar scaling for the mass-loading factor, $\eta \propto v_{\rm c}^{-2.2}$.

One key issue is that M15 report their results at R_{25}, one quarter of the virial radius, while by necessity we impose our wind scalings at wind launch, which occurs inside star-forming regions within the galaxy at much smaller radii. Clearly, it makes more sense to talk about galactic wind properties outside the galaxy and R_{25} is a reasonable radius to choose. As we discuss below, M15 motivated us to look at our wind scaling properties at R_{25}, and we find that they are very different from those at launch.

Motivated by this recognition, in this paper we revisit the basic assumptions made in our subgrid wind model. In particular, we recalibrate our prescriptions for launching winds from galaxies using the scaling relations found in the FIRE simulations as constraints. We will examine how the new prescription, now capable of qualitatively reproducing the wind behaviours seen in the FIRE simulations, will affect some of the basic predictions of our cosmological simulations, such as the galactic stellar mass functions (GSMFs) and

the galactic mass–metallicity relation (MZR) at various redshifts. Furthermore, we also experimented with a range of wind parameters, all allowed by current observational and theoretical constraints on galactic winds, to examine the robustness of these predictions to small changes in the wind implementation and were surprised to find that these basic observational quantities were actually very sensitive to small changes in the wind scalings, changes that are much smaller than the differences between wind models employed by different simulation groups (e.g. Agertz et al. 2013; Schaye et al. 2015; Davé, Thompson & Hopkins 2016; Pillepich et al. 2018a).

Recent cosmological simulations also often adopt a subgrid active galactic nucleus (AGN) feedback model and show that it is crucial to reproduce the number density of massive galaxies and the fraction of red galaxies at low redshifts to match observations. The simulations presented in this paper, like our past published work, do not include any such subgrid model for AGN feedback, or any other mechanism that has been proposed in the literature to specifically quench star formation in massive galaxies (e.g. Crain et al. 2015; Davé et al. 2016; Weinberger et al. 2016). Simulations without AGN feedback tend to produce too many blue massive galaxies, indicating that the stellar feedback alone is insufficient to keep these galaxies quenched. However, the implementation of AGN feedback often has little effect at higher redshift or in small galaxies, where stellar feedback dominates galaxy growth. The implementation of any AGN feedback model that includes free parameters that are tuned to match observations will thus inevitably be affected by the stellar feedback models. Therefore, in this paper we will not focus on reproducing the observed Universe in every detail, but we will rather explore how sensitively galaxy evolution depends on the star formation-driven wind model. This knowledge will also help characterize the limits of what stellar feedback alone can accomplish and thus provide further constraints on any additional required feedback mechanism.

The paper is organized as follows. Section 2 reviews our original subgrid model for launching winds in our simulations and also introduces the new wind algorithm. Section 3 describes our cosmological simulations and introduces the test simulations that we use in this paper. Section 4 studies how sensitively our simulations depend on the parameters of the wind algorithm by comparing results from the test simulations. Section 5 studies in detail how stellar mass grows within galaxies in our simulations by focusing on their accretion and merger histories, and how it is affected by certain wind parameters. It also discusses the challenge of matching observations relying only on stellar-driven winds and the requirements for any additional feedback mechanism. Section 6 presents results from our high-resolution simulation using the new wind algorithm with a fiducial choice of wind parameters and compares them to results from earlier published versions of our cosmological simulations. Section 7 summarizes our results.

2 THE KINETIC FEEDBACK MODEL

2.1 Our published wind model

We based our original subgrid wind model (*ezw*; Davé et al. 2013; Ford et al. 2016) on the analytic formulation of energy-driven and momentum-driven winds from Murray et al. (2005). Here we summarize our numerical algorithm for including it in our simulations. For any SPH particle i in a galaxy that is above a critical density threshold $\rho_{\rm SF}$ for star formation, we determine whether or not to turn it from a normal SPH particle into a wind particle according to a probability p_i that scales with the local SFR:

$$p_i \propto \eta \times {\rm SFR}_i.$$

We choose the critical density threshold as $\rho_{\rm SF} = 0.13\,\mu m_{\rm H}$ (Springel & Hernquist 2003), where μ is the mean atomic weight and $m_{\rm H}$ is the mass of the hydrogen atom. Once an SPH particle becomes a wind particle, we add a velocity boost of $v_{\rm w}$ to the particle in the direction of $\boldsymbol{v_i} \times \boldsymbol{a_i}$, where $\boldsymbol{v_i}$ and $\boldsymbol{a_i}$ are the velocity and acceleration of the particle, respectively, before launch, as outflows are often seen perpendicular to the disc where the resistance from the cold dense ISM is minimized. All hydrodynamical interactions relating to the newly created wind particle are ignored for an interval of $t_{\rm delay} = 20\,{\rm kpc}/v_{\rm w}$ or until the particle has reached a density threshold of $\rho_{\rm th} = 0.1\rho_{\rm SF}$. This decoupling from hydrodynamical forces ensures that wind particles are able to escape the disc where the resolution is insufficient to correctly model the hydrodynamical interactions (Dalla Vecchia & Schaye 2008). The two free parameters, η and $v_{\rm w}$, are crucial to the wind model, whose values are constrained from the analytical scalings that correlate them with the galaxy velocity dispersion σ. For our preferred published model (Davé et al. 2013), which we refer to as the *ezw* model, those scalings are as follows:

$$v_{{\rm w};ezw} = 4.29\sigma\sqrt{f_{\rm L} - 1} + 2.9\sigma \tag{2}$$

$$\eta = \begin{cases} \dfrac{150\,{\rm km\,s^{-1}}}{\sigma}\dfrac{75\,{\rm km\,s^{-1}}}{\sigma} & (\sigma \leqslant 75\,{\rm km\,s^{-1}}) \\ \dfrac{150\,{\rm km\,s^{-1}}}{\sigma} & (\sigma \geqslant 75\,{\rm km\,s^{-1}}) \end{cases}, \tag{3}$$

where $f_{\rm L}$ depends on the metallicity of the SPH particle as constrained by observations (Rupke et al. 2005), and we adjust the normalization factor $\sigma_0 = 150\,{\rm km\,s^{-1}}$ to match the enrichment level of the high-redshift IGM (Oppenheimer & Davé 2008).

This original wind velocity formula (equation 2) rescales the launch wind velocity by adding 2.9σ in an attempt to get the correct asymptotic velocity at the virial radius, to account for the dynamical evolution of the winds inside the halo. However, as we will show in Section 3.1, this does not work very well.

The formula for η introduces a characteristic velocity $\sigma_{ezw} = 75\ {\rm km\,s^{-1}}$ that separates the momentum-driven wind scaling regime from the energy-driven one. The momentum-driven mass-loading factor, which scales with σ^{-1}, applies to relatively large systems where outflows could be driven primarily by the momentum flux from young stars and SNe while the thermal energy from SNe would be dissipated too quickly to become dynamically important. However, in dwarf galaxies with σ below this limit, we assume that energy feedback from SNe starts to dominate, based on analytical and numerical models by Murray, Quataert & Thompson (2010) and Hopkins, Quataert & Murray (2012). In this energy conserving regime, we assume $\eta \propto \sigma^{-2}$. Whether or not the physical models behind these scaling relations are correct, Davé et al. (2013) show that this hybrid scaling leads to better agreement with both the low mass stellar mass and H I mass functions at $z = 0$.

We determine the velocity dispersion σ of the host halo on the fly. We identify galaxies using a friends-of-friends (FoF) algorithm that binds star-forming particles to their closest neighbours. We estimate the velocity dispersion using the total mass of the galaxy $M_{\rm gal}$:

$$\sigma_{\rm FoF} = 200\left(\frac{M_{\rm gal}}{5\times10^{12}\,{\rm M_\odot}}\frac{H(z)}{H_0}\right)^{1/3}\ {\rm km\,s^{-1}}, \tag{4}$$

where $M_{\rm gal}$ is the total mass of the FoF group, and $H(z)$ and H_0 are the Hubble constants at redshifts z and 0, respectively. $M_{\rm gal}$ includes

dark matter, gas, and stars and we choose the FoF linking length to be smaller than one that would make $M_{\rm gal}$ equal to the virial mass (see Section 2.3 for details). In principle, we could measure the velocity dispersion $\sigma_{\rm FoF}$ for each galaxy directly. However, uncertainties arise owing to poor resolution particularly in the inner regions of each galaxy (Oppenheimer & Davé 2006). Moreover, the numerical noise would in some cases yield an unrealistic $\sigma_{\rm FoF}$ that would lead to unphysical results. Finally, satellite galaxies often have their $\sigma_{\rm FoF}$ overestimated owing to contamination by particles that actually belong to the central galaxy but that are impossible to separate. Therefore, we use the above empirical relation given that any error that arises from using this relation is subdominant to the uncertainties that come from our assumptions about the wind model itself.

2.2 A new algorithm for launching winds

The wind speed formula above (equation 2) derives from the analytic calculations of Murray et al. (2005) (equation 1 in this paper) for radiation-driven winds. However, as discussed in the introduction, the actual propagation of wind particles in SPH simulations is very different from that assumed in this analytic model. In the simulations, a wind particle is initially decoupled from the hydrodynamics until it reaches the critical density $\rho_{\rm th}$, typically several kiloparsecs from the galactic centre. After that, the particle can interact hydrodynamically with the surrounding gas and will slow down and heat. How this occurs depends on the numerical details of the hydrodynamic solver, since the interaction is poorly resolved. In dwarf galaxies, the winds are typically much faster than the escape velocity and are able to escape their host haloes, but most winds in massive galaxies only travel to a certain distance from the galaxy and eventually fall back within a recycling time-scale $t_{\rm rec}$ (Oppenheimer et al. 2010). We will show in Section 4 that both the distances to which wind particles travel and their recycling time-scales are highly sensitive to the initial wind speed and numerical resolution. This leads to large uncertainties in the evolution of galaxies and their CGM properties because the behaviour of the ejected wind particles has a crucial impact on the gas supply for star formation inside galaxies, and the density, temperature, and metal distribution in the surrounding halo gas.

Here we present an improved algorithm to determine how winds are ejected from their host galaxies. In this new method, we keep the velocity of a wind particle relative to its host galaxy constant until it reaches the density threshold $\rho_{\rm th}$ where the particle recouples hydrodynamically to the other gas. We choose the density threshold to be 0.1 $\rho_{\rm SF}$, where $\rho_{\rm SF}$ is the physical density threshold above which star formation occurs in the simulation. Therefore, before recoupling, the wind particle effectively also decouples from gravity so that its kinetic evolution remains temporarily independent of the central potential dominated by baryons. The wind particle still contributes to the overall gravitational field as it leaves the disc, preventing galaxies with strong outflows from having large artificial dynamical disturbances in the disc.

We also adopt a new formula for the initial wind speed that is parametrized differently from before. As we will see in Section 3.1, this results in $v_{\rm w} \propto v_{\rm c}$ at R_{25} as found in M15 and Murray et al. (2005). We keep the tangential velocity relative to the galaxy fixed so that the wind particle conserves its angular momentum as it is launched. We determine the radial component of the velocity by

$$v_{\rm w} = \alpha_v \sigma \sqrt{f_{\rm L}} \left(\frac{\sigma}{50\ {\rm km\ s^{-1}}}\right)^{\beta_v}, \quad (5)$$

where α_v and β_v are free parameters that will be discussed later, and $f_{\rm L}$ is the metallicity-dependent ratio between the galaxy luminosity and the Eddington luminosity. We adopt the Oppenheimer & Davé (2006) formula for $f_{\rm L}$:

$$f_{\rm L} = f_{\rm L;\odot} \times 10^{-0.0029(\log Z_{\rm gal}+9)^{2.5}+0.417\,694}, \quad (6)$$

where $f_{\rm L;\odot}$ varies randomly between 1.05 and 2. Here we now use the mass-weighted average metallicity $Z_{\rm gal}$ of the host galaxy to compute $f_{\rm L}$, instead of directly using the metallicity of the wind particle as in their paper and in our past work. This is more appropriate since it is the global properties of the galaxy that will determine the wind properties at R_{25} and the metallicities may have large variances inside a galaxy. In most galaxies, $f_{\rm L}$ is only slightly above 1. Note that the $\sqrt{f_{\rm L}-1}$ term in the original *ezw* velocity formula (equation 2) becomes $\sqrt{f_{\rm L}}$ after adding in the kinetic energy lost to the gravitational field as the wind particle climbs up the potential, so that our winds can match the asymptotic velocity predicted by equation (1). In the original formula, this correction is included as the second term 2.9σ, which is normalized at a radius of $R_{\rm esc} = 0.1R_{\rm vir}$. Note that this is different from the R_0 that appears in the analytic formula (equation 1). Oppenheimer & Davé (2006) chose $R_0 = 0.01R_{\rm vir}$ to obtain the constant factor 4.29 in the first term of equation (2). In our new formula, we use the same normalization radius $R_{\rm esc} = R_0$ for the two terms. We incorporate the freedom of choosing R_0 into the parameter α_v.

The parameters α_v and β_v determine the overall wind speed and its scaling with the depth of the halo potential. Since σ scales with $M_{\rm gal}^{1/3}$, the wind speed scales with the halo mass by a power-law index $(1+\beta_v)/3$. The parameter β_v, therefore, characterizes how much momentum the wind particles need to overcome the central, baryon-dominated gravitational potential and reflects how the central potential varies with halo mass. The parameter α_v reflects the uncertainties in choosing the normalization radius R_0 in equation (1) and in measuring the σ from simulations. We calibrate our parameters to make our wind scalings at R_{25} consistent with the results from M15 (see Section 3.1 for details). Note that this wind speed should not be directly compared with observations because this wind speed formula only applies to winds that are close to the disc (R_0), where they are launched, while observationally the location of the winds is usually unknown.

In addition to the wind speed, we also explore different choices for the mass-loading factor scalings. Instead of the original formula (equation 3), we now parametrize η as

$$\eta = \begin{cases} \alpha_\eta \left(\dfrac{150\ {\rm km\ s^{-1}}}{\sigma}\right) \left(\dfrac{\sigma_{ezw}}{\sigma}\right)^{\beta_\eta} (1+z)^{1.3} & (\sigma \leqslant \sigma_{ezw}) \\ \alpha_\eta \left(\dfrac{150\ {\rm km\ s^{-1}}}{\sigma}\right) (1+z)^{1.3} & (\sigma \geqslant \sigma_{ezw}) \end{cases}, \quad (7)$$

where α_η is a normalization factor and β_η is the power-law index.

Therefore, the mass-loading factor η still follows a momentum-driven wind scaling $\eta \propto \sigma^{-1}$ in massive systems above a certain threshold σ_{ezw}. Below that threshold, $\eta \propto \sigma^{-(1+\beta_\eta)}$. The original energy-driven scaling in small galaxies corresponds to $\beta_\eta = 1$. However, we will show in later sections that to match the observed number densities of small galaxies at high redshifts requires a higher β_η value. We also adopt a redshift-dependent factor $(1+z)^{1.3}$ motivated by the results from the FIRE simulations (M15). To avoid unphysically large η at high redshifts, we only allow η to change with z at $z < 4$ and use a constant factor of $5^{1.3}$ at $z > 4$.

2.3 The FoF group finder

Both the mass-loading factor and the wind speed in our wind algorithm depend on the properties of the galaxy from which the winds are launched. To identify galaxies and their host haloes on the fly, we use an FoF group finder with a linking length of 0.04 times the mean interparticle spacing, and multiply the resulting mass by a constant factor determined via a calibration against the results from using SO, a more accurate but more computationally costly spherical overdensity halo finder (Kereš et al. 2005; Huang et al. 2019). Above the mass resolution limit, the on-the-fly FoF group finder typically underestimates the total mass (including both baryons and dark matter) by a factor of 2–3 with a scatter of ∼0.1 dex. The discrepancies between the estimated halo masses are nearly scale independent, introducing only a small additional factor of $\sigma^{0.05}$ to the wind scalings (equations 5 and 7).

Furthermore, we now identify the group centre and velocity centroid by including all cold baryons (including star-forming gas and stars) within the FoF group instead of just using stars as in our previous work. This is especially important for dwarf galaxies that have only begun assembling, which can be almost devoid of stars.

2.4 Wind energy

In this section, we calculate the total kinetic energy flux of the star formation-driven winds according to our new wind speed formula (equation 5). For a total mass M_* of stars formed, the total kinetic energy added to the winds that are generated as a consequence is

$$E_{\rm kin}(M_*) = \frac{1}{2} M_{\rm w} \bar{v}_{\rm w}^2, \tag{8}$$

where the amount of winds launched over a given time $M_{\rm w}$ relates to the amount of star formation by $M_{\rm w} \equiv \eta M_*$, and $\bar{v}_{\rm w}$ is the average wind speed. Combining this equation with the definition of η and $v_{\rm w}$ results in

$$E_{\rm kin} = 0.7 \bar{f}_{\rm L} \alpha_v^2 \sigma^2 \left(\frac{106}{\sigma}\right)^{\beta_\eta - 2\beta_v + 1} (1+z)^{1.3} M_*, \tag{9}$$

where $\bar{f}_{\rm L} \sim 1.0$ is the average value for the luminosity factor that appears in equations (1) and (5). Therefore, the wind energy generated per solar mass of star formation is

$$\begin{aligned} E_{\rm kin}({\rm M}_\odot) = {} & 1.6 \times 10^{47} \\ & \times \alpha_v^2 (2.1)^{2\beta_v} \left(\frac{106}{\sigma}\right)^{\beta_\eta - 2\beta_v - 1} \\ & \times (1+z)^{1.3} \ {\rm erg}. \end{aligned} \tag{10}$$

Using the parameters for our fiducial simulation: $\alpha_v = 4.0$, $\beta_v = 0.6$, and $\beta_\eta = 4.0$, the wind energy for massive galaxies with $\sigma > 106\,{\rm km\,s^{-1}}$ is

$$E_{\rm kin}({\rm M}_\odot) = 6.3 \times 10^{48} \left(\frac{106}{\sigma}\right)^{-2.2} (1+z)^{1.3} \ {\rm erg}. \tag{11}$$

One can compare this value to the amount of energy available from Type II SNe. According to a Chabrier IMF, the average number of type II SNe per one solar mass is $\eta_{\rm SN} = 8.3 \times 10^{-3}$. Assuming each SN produces $E_{\rm SN} = 10^{51}$ erg of energy, the total energy produced by SN per solar mass of stars formed is $\epsilon_{\rm SN} = 8.3 \times 10^{48}$ erg. In our new wind model, this equals the wind energy from a galaxy at $z = 0$ with $\sigma_{\rm FoF} \sim 120\,{\rm km\,s^{-1}}$. After taking into account the factor of $\sim 3^{1/3}$ underestimate of the real σ by the on-the-fly FoF finder and using $v_{\rm c} = \sqrt{2}\sigma$, this corresponds to a circular velocity of $v_{\rm c} \sim 240\,{\rm km\,s^{-1}}$. For lower mass galaxies, the wind energy is a fraction (<1) of the energy available from SNe, but for massive galaxies it is larger.

Hence, in addition to equation (5), we adopt an upper limit for the wind speed that requires the total kinetic energy of winds to be less than 5 times the total available energy from type II SNe. Of course, in these more massive systems one expects the winds to be dominated by photon momentum if one takes the model seriously. Even so, we think it prudent to limit the total wind energy. The calculation above shows that the upper limit only matters at high redshifts or in the most massive systems.

3 SIMULATIONS

We implemented the new wind algorithm into our SPH code based on GADGET-3 [see Springel (2005) for reference]. The code includes several recent numerical improvements in the SPH technique (Huang et al. 2019). To summarize, we use the pressure–entropy formulation (Hopkins 2013) of SPH to integrate the fluid equations and a quintic spline kernel to measure fluid quantities over 128 neighbouring particles. We also use the Cullen & Dehnen (2010) viscosity algorithm and artificial conduction as in Read & Hayfield (2012) to capture shocks more accurately and to reduce numerical noise. Both the artificial viscosity and the conduction are turned on only in converging flows with $\nabla \cdot \boldsymbol{v} < 0$ to minimize unwanted numerical dissipation. We also include the Hubble flow while calculating the velocity divergence. Our fiducial code leads to considerable improvements in resolving the instabilities at fluid interfaces in subsonic flows and produces consistent results with other state-of-art hydrodynamic codes in various numerical tests (Sembolini et al. 2016a, b; Huang et al. 2019).

In the current version, we also add metal-line cooling including photoionization effects for 11 elements as in Wiersma, Schaye & Smith (2009), and we recalculate cooling rates according to an updated ionizing background (Haardt & Madau 2012). The star formation processes are modelled as in Springel & Hernquist (2003), which includes a subgrid model for the multiphase ISM in dense regions with $n_{\rm H} > 0.13\,{\rm cm^{-3}}$, and a star formation recipe that is scaled to match the Kennicutt–Schmidt relation. In this paper, we will distinguish SPH particles as star forming or non-star forming based on whether or not their densities are higher than this density threshold. We specifically trace the enrichment of four metal species C, O, Si, and Fe that are produced from type II SNe, type Ia SNe, and AGB stars as in Oppenheimer & Davé (2008). These processes also generate energy that we put in the simulations with subgrid models. However, the input energy from these feedback processes only has subdominant effects to galaxy formation compared to the wind feedback (Oppenheimer & Davé 2008).

We evolve the fiducial simulation (RefHres) for this paper in a comoving periodic box with $L = 50\,h^{-1}$ Mpc on each side that initially contains 2×576^3 gas and dark matter particles. The initial masses of each gas particle and dark matter are $m_{\rm gas} = 1.1 \times 10^7\,{\rm M}_\odot$ and $m_{\rm dark} = 6.6 \times 10^7\,{\rm M}_\odot$, respectively. Our Plummer equivalent gravitational softening of 1.2 kpc determines our spatial resolution. In addition, we run several simulations with the same initial conditions in $L = 50\,h^{-1}$ Mpc boxes but at a lower resolution with 2×288^3 particles (with eight times worse mass resolution and two times worse spatial resolution). Most of these simulations use the same wind algorithm as in the fiducial simulation with only differences in the wind parameters. We use these simulations to test the numerical convergence of the wind algorithm and also to determine the sensitivity of the simulations to the wind parameters.

Table 1. Simulations and their wind parameters.

Simulation	α_η	β_η	σ_{ezw} [a]	α_v	β_v [b]	Colour[c]	Remark
RefHres	0.1	4	106	4.0	0.6	black	Fiducial wind model, high resolution with $N_{\rm gas} = 576^3$
Ref	0.1	4	106	3.5	0.6	magenta	Fiducial wind model, $N_{\rm gas} = 288^3$
ezw	4.29	1	75	–	0.0	dark red	The *ezw* model from Davé et al. (2013)
ezwFast	4.29	1	75	3.5	0.6	teal	*ezw* mass loading, but wind speeds of Ref
ezwDESPH	4.29	1	75	–	0.0	blue	The *ezw* wind model, traditional SPH methods
StrongFB	0.2	4	106	3.5	0.6	red	$\alpha_\eta = 0.2$ instead of the fiducial value 0.1
WeakFB	0.05	4	106	3.5	0.6	orange	$\alpha_\eta = 0.05$ instead of the fiducial value 0.1
Sigma75	0.4	4	75	3.5	0.6	brown	$\sigma_{ezw} = 75\,{\rm km\,s^{-1}}$ instead of the fiducial $106\,{\rm km\,s^{-1}}$
Refσ4	0.1	3	106	3.5	0.6	steel blue	η scales with σ^{-4}, not $\eta \propto \sigma^{-5}$ as in Ref
Refσ3	0.1	2	106	3.5	0.6	plum	η scales with σ^{-3} not $\eta \propto \sigma^{-5}$ as in Ref
RefSlow	0.1	4	106	3.0	0.3	green	Same as the Ref simulation but slower winds

Notes. [a]The first three parameters, α_η, β_η, and σ_{ezw} determine the mass-loading factor according to equation (7). The *ezw* wind model uses a slightly different formula (equation 3) where these parameters have a similar effect.
[b]The next two parameters, α_v and β_v, determine the initial wind speed according to equation (5). The wind speed in the *ezw* model is formulated in a quite different way so that the parameters do not apply.
[c]We use a consistent colour scheme for the entire paper to distinguish simulations from each other. This column indicates the unique colour that is used to represent the corresponding simulation.

We choose the $50\,h^{-1}$ Mpc size to balance between a decent numerical resolution and a representative volume, given the computational resources that are feasible. Furthermore, many of our previous results are based on simulations of similar volume and resolution. We are therefore able to verify the robustness of these previous results with the volume chosen. Zoom-in simulations (e.g. Sadoun et al. 2016; Valentini et al. 2017) provide a wide range of observables and diagnostics different from those probed by cosmological simulations and are therefore complementary to this study.

In Table 1, we summarize and classify all the simulations into three categories. The first category simulations differ from the fiducial simulation only in terms of the mass-loading factor. The second category simulations differ only in terms of wind speed. In Section 4, we will focus on comparing simulations of each category to demonstrate the sensitivity to the wind parameters. The rest of the simulations differ in both the mass-loading factor and the wind speed or use different wind algorithms such as our original hybrid *ezw* wind model. In addition, the ezwDESPH simulation is the only simulation that uses the traditional SPH technique and, therefore, is the simulation that is closest to the original numerical model used in our previously published simulations (e.g. Davé et al. 2013; Ford et al. 2016). In Section 6, we will focus on results from the fiducial simulation and compare them to observations as well as the original *ezw* model to show how much the new fiducial wind algorithm changes some of our basic results from our previous simulations.

To illustrate how differences in the mass-loading factors affect the simulations, we show in the upper panel of Fig. 1 the input scaling laws (equation 7) between the mass-loading factor η and the velocity dispersion σ measured from the on-the-fly FoF group finder. In the lower panel, we show the actual mass-loading factor of individual galaxies in each simulation as a function of their stellar mass at $z = 2$. For comparison, we also show the empirical fit from the FIRE simulations (M15), and a formula used in the Somerville et al. (2012) semi-analytic model.[1] When making these comparisons, remember, however, that the η referred to in the simulations is at wind launch inside the galaxy while the η values in the FIRE simulations are measured well outside the galaxy (R_{25}).

[1]Since Somerville et al. (2012) parametrizes η as a function of halo mass, we used the SMHM relation at $z = 2$ from Behroozi, Wechsler & Conroy (2013) to obtain the halo mass from the stellar mass for any galaxy.

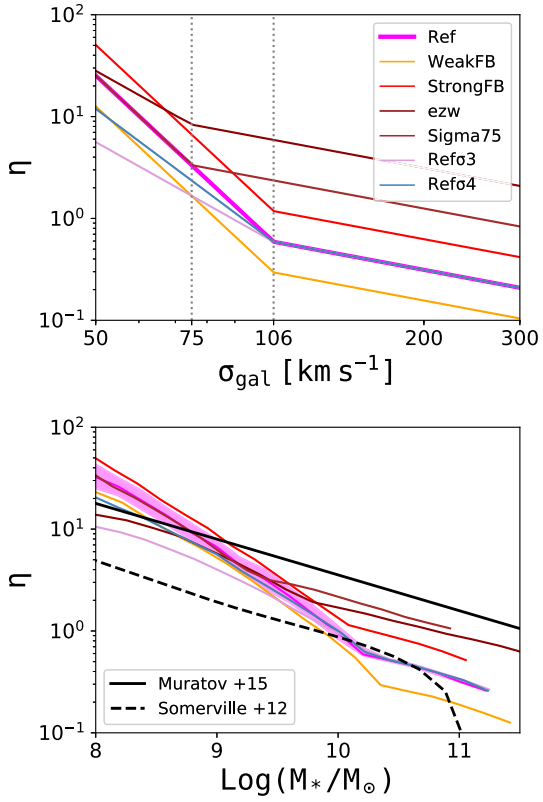

Figure 1. *Upper panels*: The mass-loading factor η, as a function of the halo velocity dispersion $\sigma_{\rm gal}$ at $z = 2$. In the simulations, we calculate $\sigma_{\rm gal}$ from the mass of each halo identified by the on-the-fly FoF group finder. The scalings follow equation (3) for the *ezw* winds and equation (7) for the new wind algorithm. *Lower panels*: η as a function of stellar mass M_*. The shaded area traces the median and includes 68 per cent of galaxies within each mass bin for the Ref simulation. Different simulations are colour coded according to Table 1. We also show the analytic formula from M15 (black solid line) and Somerville et al. (2012) (black dashed line) for comparison.

3.1 Wind speed at R_{25}

A major update to our fiducial simulation from our original *ezw* model (Davé et al. 2013) is the readjustment of the initial wind velocity so that we approximately have $v_{\rm w} \propto \sigma$ outside the galaxy

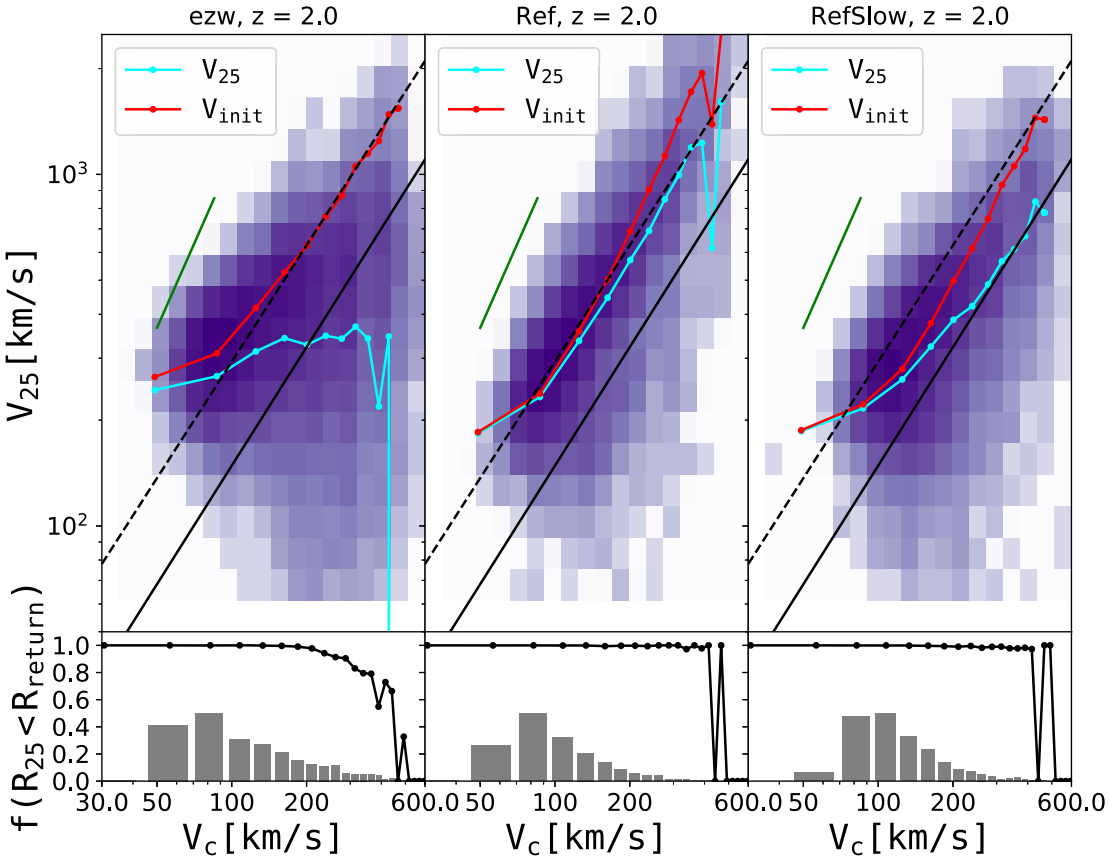

Figure 2. *Upper panels*: The relation between the velocity of wind particles and the circular velocity v_c of their host galaxy. These wind particles are launched within a small redshift window at $z = 2$. In each panel, the red line shows the running medians of the initial launch velocities and the cyan line shows v_{25} – the velocities of the wind particles when they reach 0.25 the virial radius (R_{25}). The green segment indicates the $v_w \propto \sigma^{1.6}$ scaling imposed at launch for the fiducial simulation. The colour map shows the distribution of wind particles according to their v_{25} and v_c. The colour scale indicates the number of wind particles in each cell. We also include the empirical fit from the FIRE simulations (M15). The black solid and dashed lines in each panel correspond to their 50th and 95th percentiles, respectively. *Lower panels*: In each panel, the black line shows the fraction of wind particles that reach R_{25} in their host halo. The grey histogram shows the unweighted distribution of v_c for all wind particles. The three panels from *left* to *right* are plotted for the ezw, Ref, and RefSlow simulations, respectively. Agreement between the cyan and black solid lines thus represents agreement between our wind launch prescription and the median FIRE results, but agreement between the cyan solid and black dashed lines may be a better measure for reasons described in the text. The new wind algorithm in our fiducial simulation is able to reproduce the trend seen in the FIRE simulations. However, winds in the original *ezw* simulations are in general too slow, particularly in massive galaxies, where only a small fraction of wind particles is able to reach R_{25} before falling back.

as opposed to at wind launch, in better correspondence with the Murray et al. (2005) model. In this section, we will characterize how this modification changes the behaviour of winds as they propagate into the halo after they have been launched. We will compare the wind behaviour to that predicted from the FIRE simulations, which follow the evolution of wind particles with more detailed physics and at higher resolution.

Using these zoom-in simulations, M15 derived an empirical relation between the wind speed at $R_{25} \equiv 0.25\,R_{vir}$ and the circular velocity v_c of the host halo from which the winds are launched. They find that the median wind speed could be fitted with

$$v_{w,50} = 0.85 v_c^{1.1} \tag{12}$$

and that the upper 95th percentile wind speed is fitted with

$$v_{w,95} = 1.9 v_c^{1.1}. \tag{13}$$

They obtain these relations from their data at high and medium redshifts but do not find apparent redshift evolution of these relations. This is very close to the $v_c^{1.0}$ in the Murray et al. (2005) model and our scaling at wind launch.

However, we want to compare with our winds not at wind launch but at R_{25}, where they are measured in M15. To measure the wind speed at R_{25} in our simulations at a given redshift, we track the evolution of all wind particles that are ejected within a small redshift bin centred at that redshift. We identify the host haloes of all these wind particles from the halo catalogue generated with the post-processing halo finder SO (Kereš et al. 2005). Then for each wind particle, we define the wind velocity at R_{25}, v_{25}, as the radial velocity of the particle when it first crosses the R_{25} of its host halo.

In the left-hand panel of Fig. 2, we compare the speed of wind particles in our original *ezw* model (ezw) to the empirical relations derived from the FIRE simulations (M15) measured at R_{25}. The *ezw* winds (cyan line) are much slower than in M15 in massive galaxies. In fact, most wind particles launched in galaxies above a certain v_c in the ezw simulation do not have sufficient initial momentum to ever reach R_{25} at all. This is more clearly illustrated in the bottom panels, which show as solid lines the fraction of wind particles that reach R_{25}. In the massive galaxies in the ezw simulation, the winds fall back on to their host galaxies within a very short

time-scale and, therefore, play little role in regulating the star formation of their host galaxies. Even though the winds were launched with $v_w \propto v_c$ (red line), their velocities are almost independent of R_{vir} at R_{25} (cyan line). It was this realization that originally motivated us to re-examine our wind model.

In the middle panel of Fig. 2, we make the same plot for our fiducial simulation (Ref). Now the distribution of wind particles from our simulation roughly agrees with the empirical scaling relations from the FIRE simulations (M15). In detail, the median velocities of our winds (cyan lines) are higher than their medians but are typically lower than their upper 95th percentile values. Most of the wind particles launched using the new algorithm are now able to reach R_{25}, even in the most massive systems.

There are caveats when directly comparing the median velocities between our simulations and FIRE. First, the nature of our winds differs from theirs. In M15, the winds are explicitly accelerated by the physical processes that they adopt in their simulations (Hopkins et al. 2012). Their winds are multiphase by nature but they do not distinguish the cold and warm phases when calculating the wind speed. In contrast, our winds are imposed on the galaxies and represent only the cold, mass loaded outflow, which cannot be self-consistently generated from the physics included in our simulations. Before reaching R_{25} where the wind speeds are measured and compared, the wind particles in our simulations have been slowing down owing to hydrodynamic interactions and gravity, while in their simulations the wind particles keep being accelerated by radiation pressure and it is not clear whether or not they have started to slow down at that radius. Therefore, the kinematic structure and the evolution of winds in our simulation are likely very different from theirs. Hence, we do not know if the comparison to FIRE would be substantially different at a different radius, e.g. R_{10} or R_{40}.

Second and more importantly, we measure the wind speeds in fundamentally different ways. M15 measure the wind speed using the flux-weighted average of all outflowing particles over a given epoch. This measurement preferentially selects particles where the outflowing flux is maximal, i.e. when the winds are strongest. Furthermore, their definition of outflowing particles includes all gas particles in the halo at that radius as long as their radial velocities are above the halo velocity dispersion, while in our simulations we only include the actual ejected wind particles in the measurement. Since in lower mass haloes the typical wind speed is much larger than the random motions of the halo component, their measurement likely underestimates the speed of the outflowing material that is actually accelerated from the galaxies. In contrast, in larger mass haloes their method could measure winds even for gas that is roughly in hydrostatic equilibrium within the halo and hence may overestimate the wind velocities (and η). Our measurement reflects the speed of the fastest outflowing particles within each halo and, therefore, should be more comparable to their 95th percentile values. In fact, if we try to measure our winds in a way more similar to that in M15, it lowers our median wind velocities to agree better with their median values.

Unlike M15's finding that the v_{25}–v_c relation is independent of redshift, in our simulations the v_{25} slightly decreases for a given v_c at lower redshifts, especially in massive haloes, even though we launch our winds with a redshift-independent initial velocity (equation 5). The winds lose more momentum as they move from the launching radius to R_{25} at low redshifts, likely owing to the combined effects of a deeper potential, enhanced hydrodynamic forces, and an underestimate of σ for massive haloes using the on-the-fly FoF group finder.

The significant differences between the wind behaviours in our simulations are particularly interesting considering that the initial wind velocities are not very different from each other. A relatively small difference in the initial wind speed at launch has a significant impact on the wind behaviour at larger radii. This indicates that this kinetic wind algorithm, which is adopted in many cosmological simulations (e.g. Springel & Hernquist 2003; Oppenheimer & Davé 2006; Agertz et al. 2013; Schaye et al. 2015; Davé et al. 2016; Hopkins et al. 2018; Pillepich et al. 2018a) as a subgrid model for stellar feedback, is very sensitive to the details of its implementation and the choice of wind parameters. We will discuss this sensitivity more in Section 4.

4 SENSITIVITY TO THE WIND MODEL

In this section, we explore the scaling laws that determine the mass-loading factor and the wind launch speed in our new wind algorithm, and study the sensitivity of our simulations to these parameters. All the test simulations we use in this section are listed in Table 1 and all have the same numerical resolution. We will explore the effects of numerical resolution in Section 6.

We identify galaxies using SKID and SO as in Huang et al. (2019) and measure the stellar mass and halo mass for every galaxy that we identify. First, we will focus on comparing the GSMFs at four different redshifts and discuss the effects of changing the mass-loading factor and the wind speed separately. In addition, we will also examine the growth of individual galaxies and how they differ among the simulations, since their different star formation histories are an immediate consequence of the wind algorithm, which controls their gas supply. To make direct comparisons between individual galaxies, we cross-match galaxies from different simulations to those in the Ref simulation based on their phase-space information. We also require matched galaxies to have a stellar mass difference smaller than 1 dex to avoid matching satellite galaxies to centrals. We define the differences of stellar masses between matched galaxies as $\Delta\log(M_*) \equiv \log(M_*) - \log(M_{*,f})$, where M_* is the stellar mass of a galaxy in a simulation and $M_{*,f}$ is the stellar mass of its matched galaxy in the fiducial simulation.

Finally, we will look at how the cosmic mean stellar density evolves with time in each test simulation. As an integrated quantity, the cosmic stellar density at different redshifts indicates whether or not a simulation produces the right amount of stars in total.

4.1 The GSMFs

The GSMFs are one of the most robust measurements from observations and have been used as an important constraint for calibrating subgrid models in cosmological simulations. To compare our simulated GSMFs with observations, we use results from multiple large galactic surveys. All of these observations assume a Chabrier (2003) IMF for their stellar mass estimate as in our simulation. Different measurements of the $z = 0$ GSMFs (e.g. Li & White 2009; Baldry et al. 2012; Bernardi et al. 2013; Moustakas et al. 2013) generally agree at the faint end up to $\log(M_*) \sim 10.5$ and start to deviate slightly from each other at higher masses. Both the choice of the aperture (Bernardi et al. 2013) and the choice of the stellar population synthesis template (e.g. Mitchell et al. 2013; Tomczak et al. 2014) contribute to relatively large uncertainties in stellar masses at the massive end. Conroy, Gunn & White (2009) estimated that the systematic error on stellar masses ranges from 0.3 dex at $z \sim 0$ to 0.6 dex at $z \sim 2$. Our choices of the observed GSMFs at $z = 0$ reflect these uncertainties. The Baldry et al. (2012) result

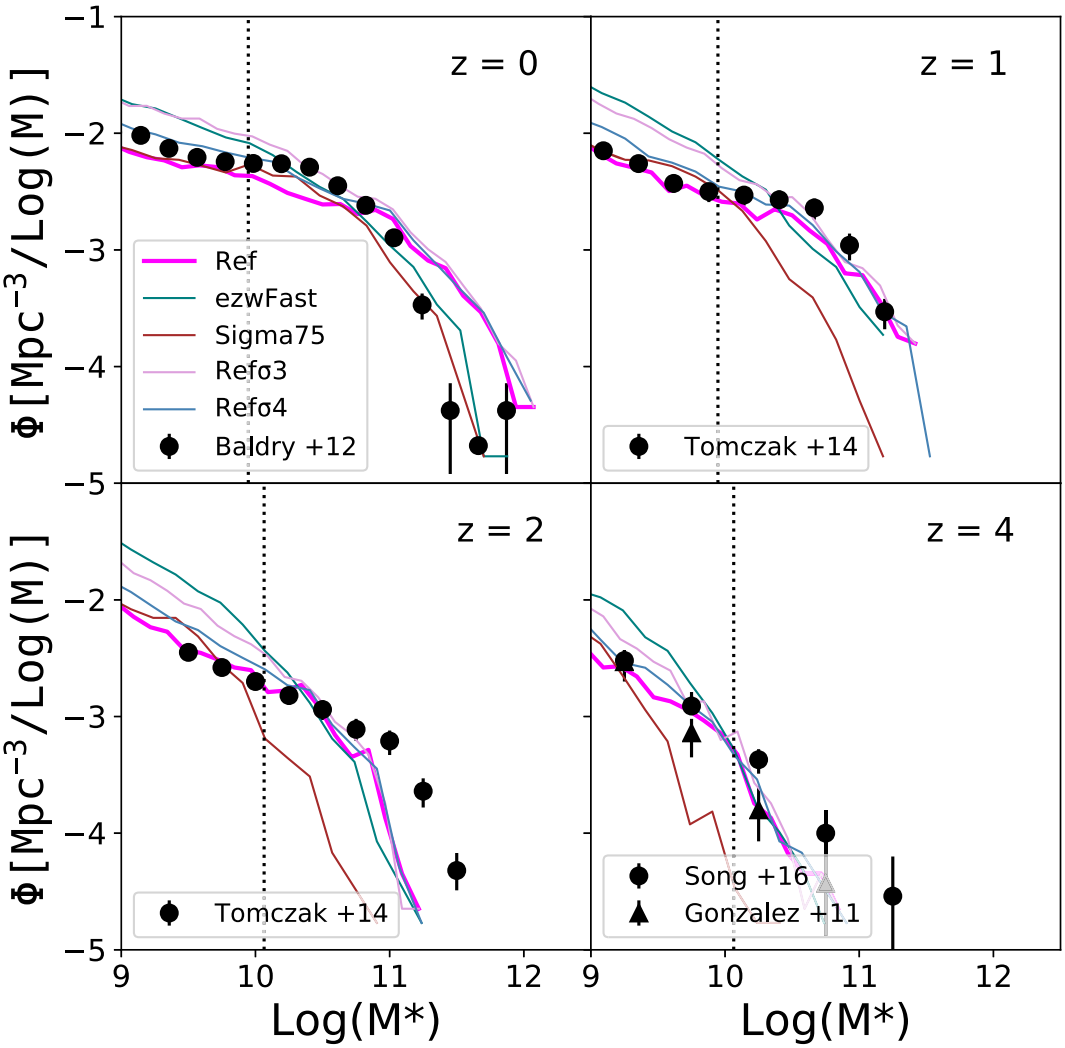

Figure 3. The GSMF at different redshifts. At each redshift, we compare the GSMFs from a set of test simulations, which are shown in different colours according to the colour scheme defined in Table 1. The dotted vertical line in each panel indicates the resolution limit for galaxies corresponding to a total mass of 128 SPH particles in these low-resolution simulations. The observational data for these redshifts are described in the text.

is based on single-Sersic fits to the light profiles of galaxies at $z < 0.06$ from the Galaxy And Mass Assembly (GAMA) survey, while Bernardi et al. (2013) use a Sersic-bulge + exponential disc model that results in larger stellar masses at the bright end. For $z = 1$ and 2 GSMFs, we use the data from Tomczak et al. (2014), who compiled GSMFs over a broad redshift range $0.2 < z < 3$ using deep observations from the FourStar Galaxy Evolution Survey (ZFOURGE) and the Cosmic Assembly Near-infrared Deep Extragalactic Legacy Survey (CANDELS), obtaining a completeness limit of $\log(M_*) \sim 9.5$. We use the Song et al. (2016) results from the CANDELS survey for comparison at $z = 4$.

First, we will show how the GSMFs are sensitive to the mass-loading factor. The mass-loading factor η is controlled by three parameters (equation 7): a normalization factor α_η, a power-law index β_η that determines how it scales with $\sigma_{\rm FoF}$, which is the velocity dispersion of the host halo identified from the on-the-fly group finder, and the characteristic velocity σ_{ezw} above which the scaling with $\sigma_{\rm FoF}$ changes from $\eta \propto \sigma^{-(1+\beta_\eta)}$ to $\eta \propto \sigma^{-1}$.

All the simulations that we use for this comparison are listed in Table 1 and use the same parameters for the wind speed as the fiducial simulation, but have different parameters for η. Here we describe the features of each simulation using the low-resolution fiducial simulation Ref as a reference. StrongFB increases the overall mass loading by a factor of 2 and WeakFB reduces it by a factor of 2. Sigma75 uses a smaller σ_{ezw} of 75 km s^{-1} than the fiducial 106 km s^{-1}, but also renormalizes α_η so that it has the same scaling with $\sigma_{\rm FoF}$ for small haloes below σ_{ezw}. Refσ4 and Refσ3 use shallower scalings with $\sigma_{\rm FoF}$ for haloes smaller than the characteristic σ_{ezw}, with a power index parameter β_η equal to 3 and 2, respectively, instead of the fiducial value of 4. ezwFast has the same mass loading as ezw but has the wind launch speed scalings of Ref, which produce faster winds. The bottom panel of Fig. 1 shows the relation between η and $\sigma_{\rm FoF}$ for these simulations.

4.1.1 *Dependence on β_η and $\sigma_{\rm ezw}$*

Fig. 3 shows how changing the power index β_η and the characteristic velocity σ_{ezw} affects GSMFs at different times. Not surprisingly, the faint end of the GSMFs is particularly sensitive to β_η. Since all these simulations except for ezwFast have the same $\eta_{\rm w}$–$\sigma_{\rm FoF}$ relation above σ_{ezw}, a higher β_η means more mass in outflows from smaller haloes and less star formation. Ref and Sigma75 are

the only simulations that successfully reproduce the observed faint end at all redshifts, and both have a strong scaling with $\eta \propto \sigma_{\rm FoF}^{-5}$ ($\beta_\eta = 4$). Simulations with a shallower dependence on $\sigma_{\rm FoF}$ tend to produce more low-mass galaxies at $z > 1$, creating a stronger tension with the observational data. For example, the ezwFast simulation shows that the shallow scaling $\eta_{\rm w} \propto \sigma_{\rm FoF}^{-2}$ predicted from the analytic momentum/energy-driven model results in too many faint galaxies formed at high redshifts.

The above result shows that a steep scaling between the mass-loading factor and the circular velocity, or equivalently the halo mass, is essential to explain the flat faint end of GSMFs at $z = 1$ and 2 when one uses a kinetic feedback model such as ours. This requirement for a strong dependence between η and σ has also been recently found in other work.[2] In the IllustrisTNG simulations, Pillepich et al. (2018b) reported a scaling with $\eta \propto M_{\rm h}^{-1} \propto \sigma^{-3}$ (see their fig. 7) as their fiducial choice to fit a wide range of observables. The FIRE simulations generate galactic outflows self-consistently instead of using a simple scaling law and found $\eta \propto \sigma^{-3.3}$ (M15). Semi-analytic studies (SAM) also require steep scalings to fit the GSMFs at different redshifts. Lu et al. (2014) reported a rather steep scaling with $\eta \propto \sigma^{-6}$. Somerville et al. (2012) parametrize their mass loading as $\eta \propto \sigma^{-\beta_{LD}}[1 + \sigma^{\beta_{EJ}}]^{-1}$ with fiducial parameters $\beta_{LD} = 2.25$ and $\beta_{EJ} = 6$. This scaling, also shown in Fig. 1, is similar in form to our scalings, though the normalization is lower. Peeples & Shankar (2011) also find with their chemical evolution model that very steep mass loading scalings ($\eta \propto v_{\rm c}^{-3}$ or steeper) are required to explain the steep slope of the observed MZR at $z = 0$. Even though the specific wind models used in these other works have important differences, such as whether or not they add additional heating, it is clear that the efficient suppression of star formation in less massive galaxies requires stronger winds than those predicted from the energy-driven model ($\eta \propto \sigma^{-2}$) or the momentum-driven model ($\eta \propto \sigma^{-1}$), which were previously assumed in many cosmological simulations. Note that the GSMF at $z = 0$ alone is insufficient to differentiate between these different scalings. Accurate measurement of the stellar content at higher redshifts could, therefore, place important constraints on the wind models.

For more massive galaxies, β_η has a less significant effect than the parameter σ_{ezw}, which determines the mass scale where the steep scaling $\eta \propto \sigma^{-(1+\beta_\eta)}$ changes to the momentum-driven wind scaling $\eta \propto \sigma^{-1}$. The Ref, Refσ4, and Refσ3 simulations have indistinguishable GSMFs above $\log(M_*) = 10.5$ in spite of their different β_η values. In contrast, the GSMFs from the ezwFast and Sigma75 simulations start showing clear differences at the massive end from the other three simulations as early as $z = 2$, indicating that the growth of massive galaxies is very sensitive to the choice of σ_{ezw}. For example, Fig. 1 shows that the mass-loading factor in the Sigma75 simulation is the same as that in the fiducial simulation at $\sigma_{\rm FoF} < 75$ km s^{-1}, but it becomes larger by a steadily increasing factor for $\sigma_{ezw} > 75$ km s^{-1} and is a factor of $\sim$4 higher in all haloes with $\sigma_{ezw} \geq 106$ km s^{-1}, our fiducial value of σ_{ezw}. As a result, the growth of massive galaxies in the Sigma75 simulation is significantly suppressed at all redshifts.

Interestingly, the ezwFast and Sigma75 simulations have the best overall agreement with the observed $z = 0$ GSMF among all these test simulations. However, they significantly underproduce the number of massive galaxies at higher redshifts. Some of the other simulations, including the fiducial simulation, agree with observations better at higher redshifts at the cost of a slight excess of the most massive galaxies at $z = 0$. We find matching the massive end of the GSMFs at both $z = 0$ and 2 simultaneously to be very challenging within our current framework for feedback. A successful feedback model must allow a rapid build-up of massive galaxies at $z = 2$ but also must account for the slow evolution of the massive end from $z = 0$ to 2 as suggested by observations. The success of our Ref model at $z \geq 1$ but failure at $z = 0$ suggests that an additional mechanism such as AGN feedback suppresses the growth of massive galaxies at low redshifts, or else that the galaxy scalings of stellar feedback change sharply at $z < 1$.

4.1.2 Dependence on the normalization α_η

Fig. 4 shows the effects of changing the linear normalization factor α_η by comparing three simulations with α_η incrementally varying by a factor of 2. In general, a higher mass loading normalization results in less stars being formed because more cold gas is ejected in galactic winds. To a rough approximation, the GSMFs of the WeakFB and StrongFB simulations are offset horizontally by a factor of 2–4 at all redshifts, with the Ref simulation mid-way between them.

Fig. 5 compares the stellar mass differences between individual, matched galaxies from these simulations. We use the fiducial simulation as the reference so that all galaxies from that simulation lie on the black horizontal line. For each galaxy in the fiducial simulation, we find its matched galaxy in the other two simulations and calculate the stellar mass differences. The medians are shown as coloured lines.

Using a simple analytic model, we could predict the stellar mass of an isolated galaxy whose growth is governed by gas outflow, star formation, and the inflow of both pristine gas and recycled winds. The equilibrium condition is

$$\dot{M}_{\rm in} + \dot{M}_{\rm rec} = \dot{M}_{\rm out} + \dot{M}_*. \tag{14}$$

This equilibrium equation is typically a good approximation in hydrodynamic simulations (Finlator & Davé 2008). Assuming that a fraction $f_{\rm rec}$ of the outflow recycles, so $\dot{M}_{\rm rec} \approx f_{\rm rec}\dot{M}_{\rm out}$, the final stellar mass of the galaxy would be

$$M_* = M_{\rm in}\left(\frac{1}{1+\eta} + f_{\rm rec}\frac{\eta}{(1+\eta)^2}\right), \tag{15}$$

where $M_{\rm in}$ is the time-integrated mass of unrecycled gas that accretes on to the galaxy. This derivation assumes a constant η and $f_{\rm rec}$ for the galaxy. However, since both of these are functions of halo mass, this assumption breaks down for galaxies that undergo a strong evolution in their halo mass such as in a major merger.

Since two matched galaxies in different simulations have similar assembly histories, gravitational potential, and outflow speeds, their $M_{\rm in}$ and $f_{\rm rec}$ should remain approximately the same, provided that the outflows do not themselves disrupt accretion or recycling. The ratio of final stellar masses between two simulations is thus determined by the different η:

$$\frac{M_{*,1}}{M_{*,2}} = \left[\frac{1 + (1 + f_{\rm rec})\eta_2}{1 + (1 + f_{\rm rec})\eta_1}\right]. \tag{16}$$

For low-mass galaxies, we can assume $\eta >> 1$ and $f_{\rm rec} \sim 0$ because winds can easily escape from their shallow gravitational

[2]In other work, the mass-loading factor is often correlated with either the halo mass $M_{\rm h}$ or a characteristic velocity that scales with $M_{\rm h}^{1/3}$, though the specific definitions for the mass and the velocity are slightly different. For consistency, we will use $M_{\rm h}$ for halo mass and σ for the characteristic velocity.

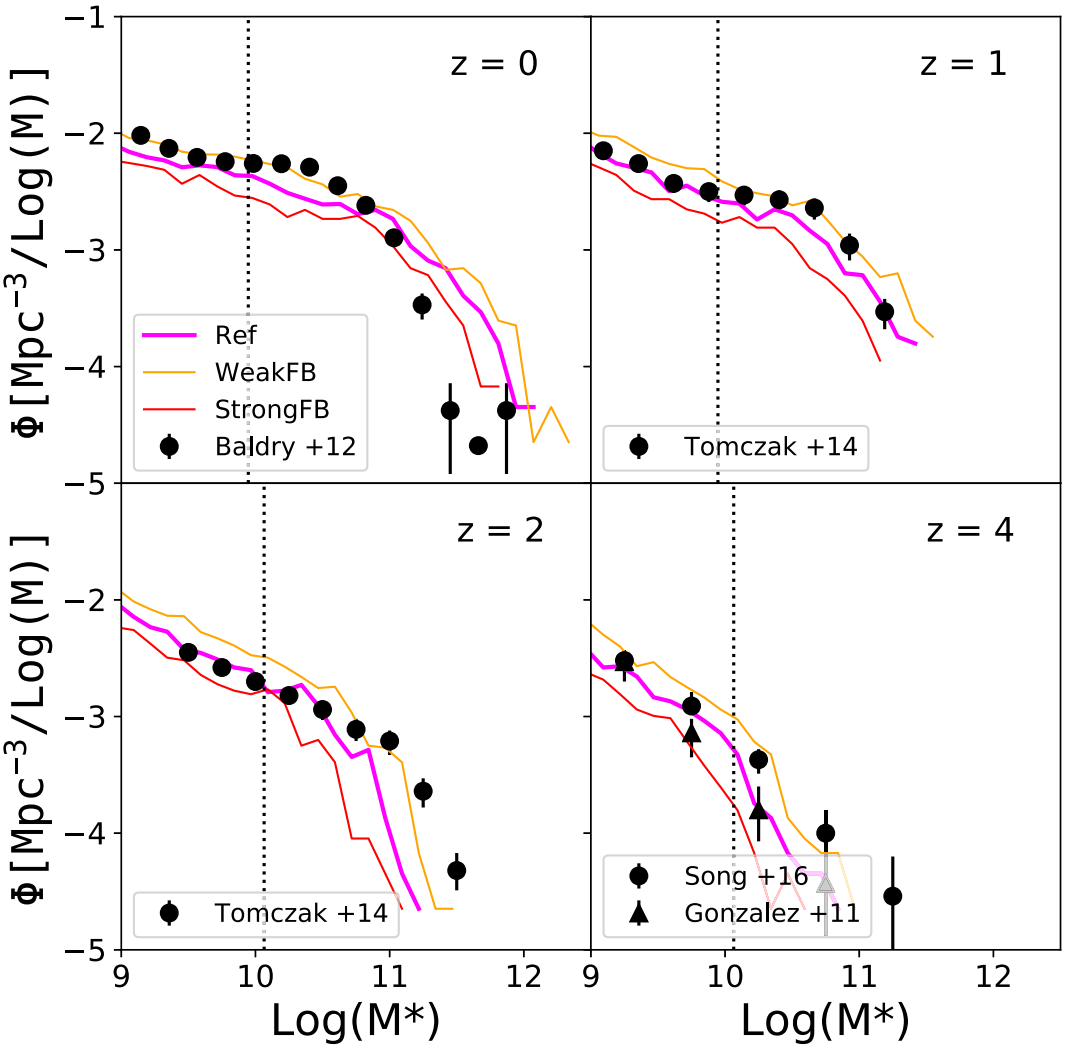

Figure 4. Same as Fig. 3, except that here we focus on the effect of the linear factor α_η of the mass-loading factor. The η in these simulations are different by a factor of 2 so that for the same galaxy, the StrongFB model (red) produces 2× more massive winds than the fiducial Ref model (magenta), while the StrongFB model (orange) produces 2× less massive winds.

potential. Hence, the ratio above will asymptotically approach

$$\left(\frac{M_{*,1}}{M_{*,2}}\right)_{\eta\gg1} = \frac{\eta_2}{\eta_1}. \tag{17}$$

Therefore, this simple model predicts that the stellar mass of small galaxies in the WeakFB and StrongFB simulations should differ from their corresponding galaxies in the fiducial simulation also by a factor of 2 (0.3 dex). Fig. 5 shows that this prediction agrees with our simulations reasonably well. It works almost perfectly when we increase η by a factor of 2. When we decrease η by the same factor, it does not work as well and the error increases with galaxy mass. This is because the approximation that $\eta \gg 1$ is less robust with decreasing η. For example, Fig. 1 shows that $\eta \sim 1$ at $\log(M_*) \sim 10$ in the WeakFB simulation. In fact, in the opposite limit, i.e. $\eta \ll 1$, equation (16) predicts that $M_{*,1} = M_{*,2}$, consistent qualitatively with the convergence of curves at high mass in Fig. 5.

The degree to which this toy model works is perhaps surprising, since it makes many oversimplified assumptions. First, the equilibrium equation (equation 14) assumes that the total amount of cold gas in galaxies does not change with time while in the simulations this is not guaranteed. Secondly, it treats galaxies in isolation, neglecting any interactions with other galaxies, but in reality a significant fraction of gas accretion may have come from previous outflows from other galaxies (e.g. Ford et al. 2014; Anglés-Alcázar et al. 2017). Thirdly, it assumes that any outflow will have no subsequent effect on the galaxy except through a nearly constant fraction of immediate wind recycling, but the outflowing gas may interact with the surrounding gas and thus affect further gas accretion. The success of the toy model suggests that these concerns are likely not dominant in our cosmological simulations.

4.1.3 Wind speed

In this section, we will show how the GSMFs are sensitive to the initial wind speed. The initial wind speed at launch depends on two parameters (equation 5): a normalization factor α_v and a power-law index β_v that determines how wind speed scales with $\sigma_{\rm FoF}$. The fiducial simulation adopts $\alpha_v = 3.5$ and $\beta_v = 0.6$. These values are tuned to match the v_{25}–v_c scaling from the FIRE simulation (M15) at $z = 2$. The ezw simulation uses the original *ezw* formula for the

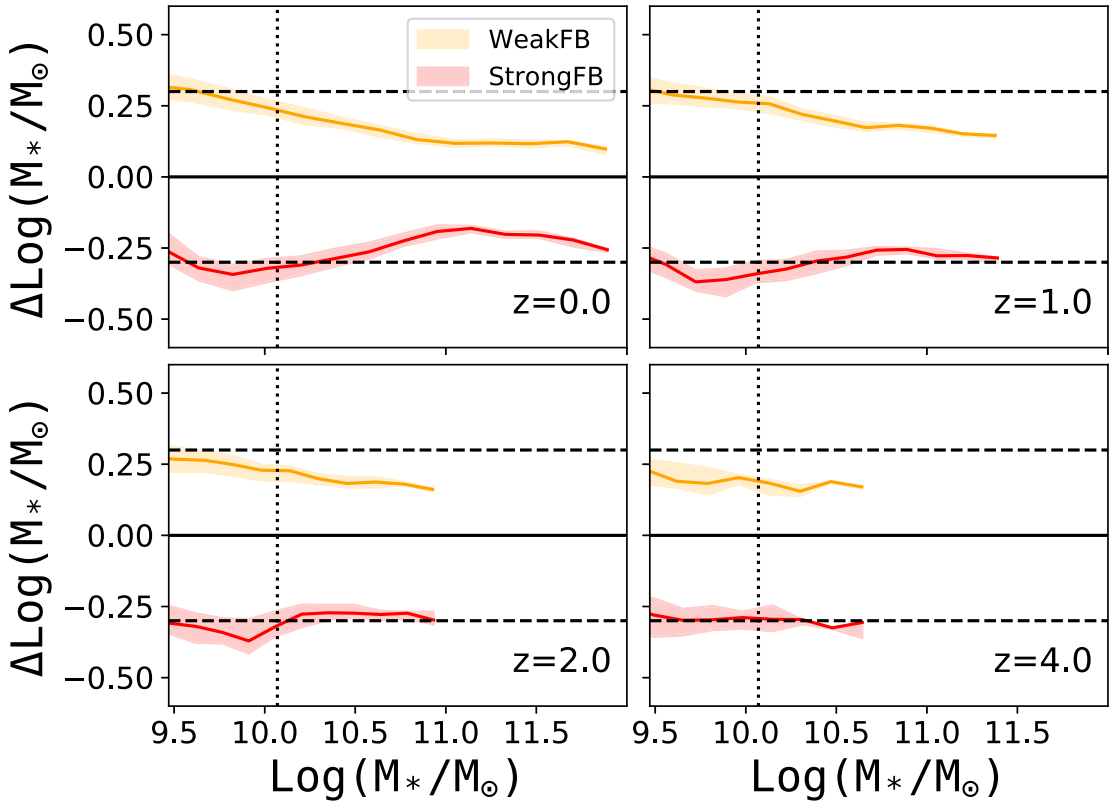

Figure 5. The stellar mass differences between galaxies that are cross-matched between the different simulations and the Ref simulation at the given redshifts. The shaded region indicates the 1σ scatter in each M_* bin. In each panel, the dotted vertical lines indicate the resolution limit of galaxies corresponding to a total mass of 128 SPH particles. The dashed horizontal lines indicate the offset in stellar masses (± 0.3 dex) predicted by equation (17).

wind speed (equation 2). The ezwFast simulation uses the fiducial wind speed scaling but the mass loading of the ezw simulation. The RefSlow simulation uses a slightly shallower slope $\beta_v = 0.5$ than the fiducial Ref simulation. Therefore, we will demonstrate the effects of wind speed by comparing the ezw and ezwFast simulations under the original η formula, and comparing the Ref and RefSlow simulations under the fiducial η formula.

Fig. 6 shows that the massive end of the GSMFs is very sensitive to the initial wind speed. First, we compare the two *ezw* simulations. At $z = 4$, the GSMFs are still very similar, because even the slower winds are above the escape velocities of haloes at this redshift. But the massive ends of the GSMFs start to show clear differences after $z = 2$. As Fig. 2 has shown, with the original *ezw* wind speed a significant fraction of wind particles fall back towards the galaxy before reaching R_{25} and become star forming again very soon after being launched. The new wind speed in the ezwFast allows wind particles to travel much further, and they return much later, if at all. This reduces the amount of stars formed in intermediate-mass haloes and at least delays stellar growth in massive haloes. As a result, galaxies in the ezwFast simulation are less massive, with the mass difference increasing towards more massive systems.

Now compare the fiducial simulation to the RefSlow simulation. The only difference between them is that the wind speed in the fiducial simulation increases slightly faster with halo mass. Even in the most massive haloes, the difference in wind speed is only a factor of 2. However, the massive galaxies in the RefSlow simulations are much more massive than those in the Ref simulation. Even more strikingly, the massive ends of the Ref and ezwFast simulations are quite close, even though their mass-loading factors at $\sigma > 106\,\mathrm{km\,s^{-1}}$ differ by a factor of $\sim$10. This similarity shows that the wind speed (matched between these simulations) is a crucial governor of high-mass galaxy growth, probably because of its impact on recycling rates.

4.2 Stellar density evolution (SDE)

In Fig. 7 we show the SDE as a function of redshift. This has been measured observationally in many studies (Li & White 2009; González et al. 2011; Baldry et al. 2012; Ilbert et al. 2013; Moustakas et al. 2013; Muzzin et al. 2013; Tomczak et al. 2014). Most of these measurements agree well within 0.1 dex at redshifts below $z = 2$, but the differences become larger at higher redshifts. Here we use the data from Muzzin et al. (2013) for redshifts 0–3 and González et al. (2011) for higher redshifts. The Muzzin et al. (2013) sample has a mass completeness limit of $\log(M_*) = 10.76$ at $z = 2.5$–3.0 and $\log(M_*) = 10.94$ at $z = 3.0$–4.0 and hence the data have to be extrapolated to estimate the stellar mass densities at these redshifts. The González et al. (2011) data can be interpreted as upper limits since they did not correct for nebular emission when using the UV data to derive the stellar densities (Smit et al. 2014).

Only the Refσ4 simulation and the fiducial simulation are consistent with the observations at all redshifts. These two simulations differ only in β_η, with the Refσ4 simulation having a shallower $\eta - \sigma$ slope $\beta_\eta = 3$ that launches less winds in low-mass galaxies. The slight excess of low-mass galaxies in the Refσ4 simulation (Fig. 3) explains its overall higher stellar densities in Fig. 7.

The simulations with a lower β_η, i.e. the ezw, ezwFast, and Refσ3 simulations, overproduce low-mass galaxies at high

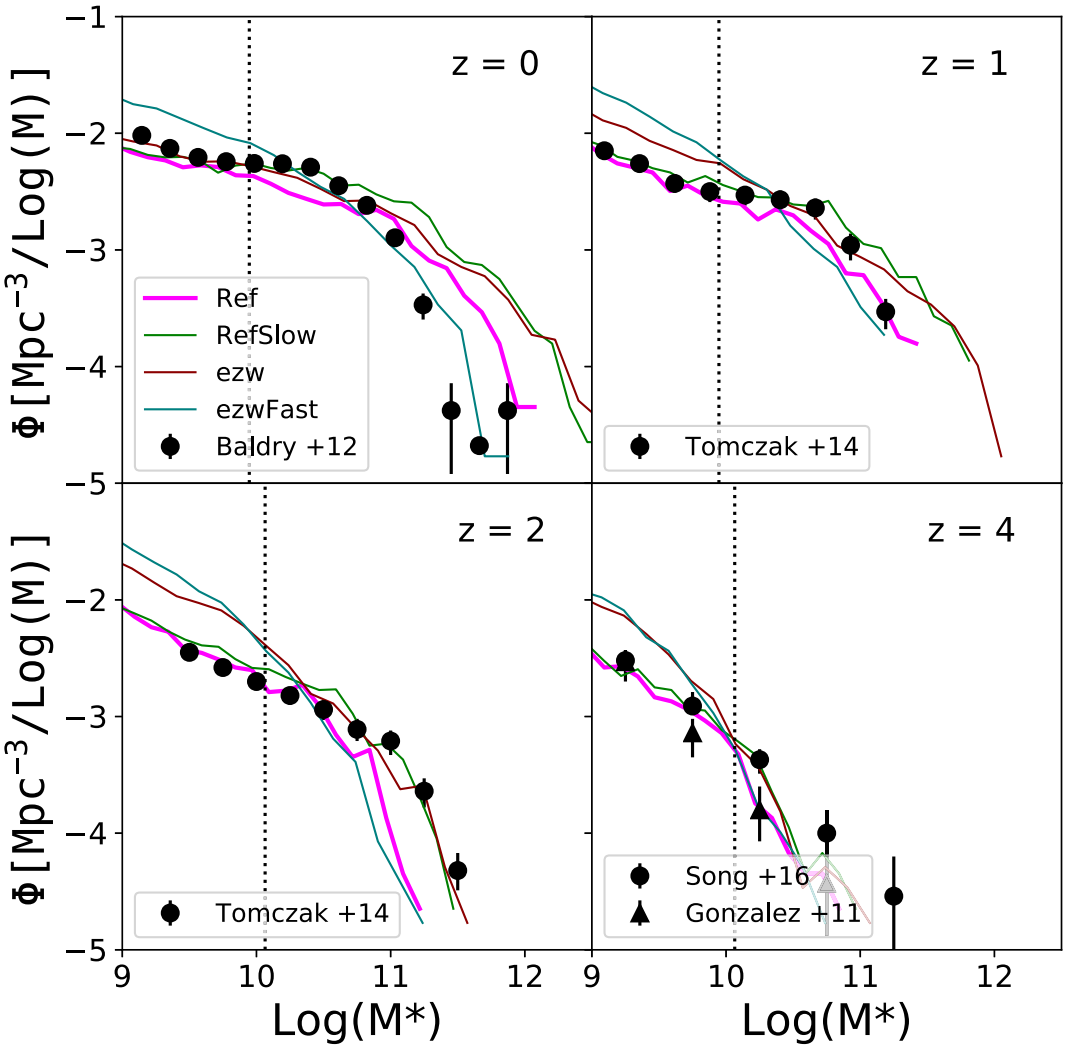

Figure 6. Same as Fig. 3, except that here we focus on the effect of different initial wind speeds on the GSMFs. The fiducial Ref (magenta) and the RefSlow (green) simulations use the new wind launch algorithm and are only different in v_w. The other two simulations use the original *ezw* wind model. However, the ezwFast (teal) simulation has fast winds as in the fiducial simulation while the ezw (dark red) simulation uses the *ezw* wind speed.

redshifts, leading to much higher stellar densities at $z > 2$. This discrepancy supports the claim in Section 4.1.1 that one requires a strong dependence of the mass-loading factor on the halo velocity dispersion.

The lower panel of Fig. 7 shows that the wind speed has a strong effect on the evolution at lower redshifts. The wind dynamics is more sensitive to the initial wind speed in massive haloes as shown in Fig. 2. The fast wind in the Ref and ezwFast simulations significantly limits the growth of massive galaxies compared to the RefSlow and ezw simulations, resulting in a slower growth of ρ_* at $z < 2$. However, ezwFast still overpredicts the total stellar mass at $z = 0$ because of too much star formation at earlier redshifts owing to a relatively smaller mass-loading factor in low-mass galaxies.

Here we have shown how the stellar content of galaxies in our simulations is sensitive to wind parameters, namely η and v_w. To make more robust comparisons to observations, we will need to further transform our simulation data into mock observations and take into account various observational effects, such as corrections for aperture (Schaye et al. 2015; Pillepich et al. 2018b) and completeness (Furlong et al. 2015). We did not make these corrections in this work as these comparisons are not meant to be interpreted as rigorous tests of our galaxy formation model, but rather to demonstrate the sensitivity of the numerical results to the wind implementations and their associated parameters.

5 DISCUSSION

In the previous section, we demonstrated that the properties of galaxies in our simulations are sensitive to the subgrid model for galactic winds. To summarize, first, the low-mass end slopes of the GSMFs are sensitive to the mass-loading factor η, especially to the power-law index β_η that determines how strongly η scales with σ in low-mass galaxies; secondly, the stellar masses of massive galaxies are sensitive to the initial wind launch speed v_w. In this section, we study in detail how galaxies build up their stellar masses in our simulations and how they are affected by the wind algorithm.

The stellar content in a given halo at any redshift is closely related to the baryon cycles (inflow/outflow) that it has experienced over cosmic time. The subgrid wind algorithm controls outflow in our simulations while the amount of cosmic accretion through filaments

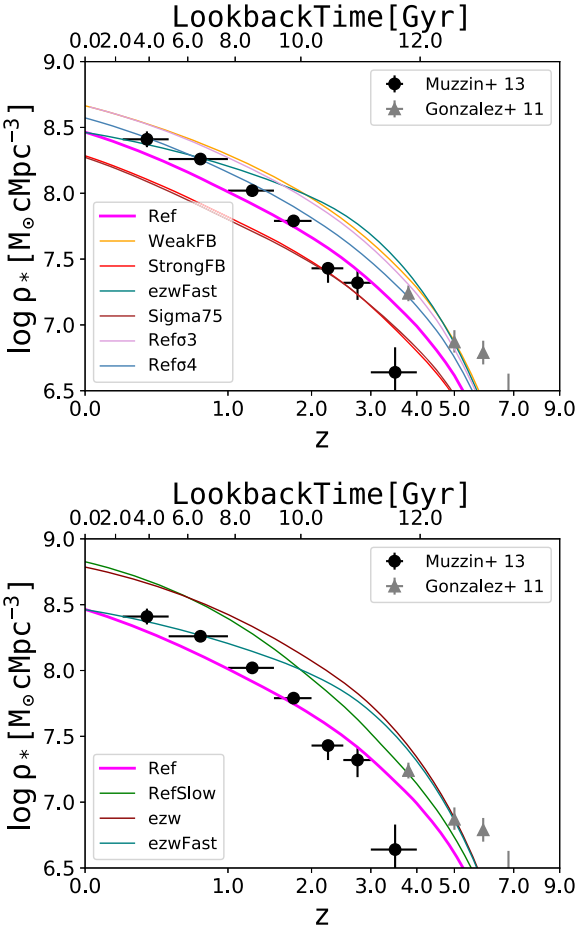

Figure 7. The evolution of the comoving stellar mass density with redshift from the test simulations. We use results from Muzzin et al. (2013) and González et al. (2011) as observational constraints, though other measurements in the literature agree with each other in general. The colour scheme for the different lines is defined in Table 1. Only the fiducial Ref and Refσ4 simulations agree with the observations. The other simulations either overproduce stars at high redshifts or fail to match the evolution at low redshifts. The *upper* panel compares simulations with different mass-loading factors. The *lower* panel compares simulations with different wind speeds.

(cold accretion) or cooling flows from the shocked halo gas (hot accretion) governs the inflow. In addition, galactic winds that were launched in the past can also fall back on to the galaxies after they lost their initial momentum. This wind recycling often dominates at low redshifts (Oppenheimer et al. 2010; Anglés-Alcázar et al. 2017). In this section, we will study the accretion history of the gas that ultimately forms stars. The particle nature of our SPH simulations makes it convenient to track the evolution of individual gas particles. In Section 5.1, we will describe how we differentiate between cold and hot primordial accretion and wind recycling through cosmic time.

We will focus on analysing and comparing three simulations: the fiducial Ref, RefSlow, and Refσ3 simulations. These simulations show clear differences in the resultant GSMFs, SDEs, and stellar mass–halo mass functions (SMHMs) at different redshifts, even though they use the same wind algorithm, albeit with different wind parameters. Using the fiducial simulation as a baseline for comparison, the RefSlow simulation represents test simulations that explore the effects of the wind speed, which we will show affects not only wind recycling but also pristine gas accretion. On the other hand, the Refσ3 simulation represents a test simulation with varying parameters for the mass-loading factor, which directly controls the amount of outflows from haloes of different masses.

In Section 5.2, we will first show how the SMHMs evolve from $z = 4$ to 0 in these simulations. In Section 5.3, we will analyse how the wind algorithms shape the SMHMs at $z = 2$ and address the differences between the simulations. Galaxy evolution at higher redshifts ($z > 2$) is much less complicated than later evolution for lower mass galaxies, since it involves various important additional processes, such as mergers, cold halo–hot halo dichotomy, and group and cluster formation. They play less significant roles at higher redshifts. However, galaxies at $z = 2$ are the building blocks for those at lower redshifts and must also agree with the observational constraints. In Section 5.4, we will focus on the late evolution after $z = 2$ and the formation histories of galaxies at $z = 0$. In Section 5.5, we will discuss the importance of mergers to the assembly of stellar mass, and in Section 5.6 we will study in detail the properties and the effects of wind recycling. Finally, in Section 5.7, we will discuss what might be missing from our feedback prescriptions and what might be needed to remove the remaining discrepancies between the simulations and the observations.

5.1 Tracking the accretion history

To understand how galaxies acquire the gas that ultimately forms their stars, we track the evolution of individual SPH particles that at some point become star forming.[3] At each time-step, we track all the accretion events, i.e. whenever a gas particle changes from non-star forming to star forming at that time-step, and output the properties of the accreted particle and the galaxy on to which it accretes. To distinguish these accretion events, we introduce a parameter $T_{\rm max}$ to characterize the thermodynamic history of the accreted particle as in Kereš et al. (2005) and Oppenheimer et al. (2010). We define $T_{\rm max}$ as the maximum temperature the particle ever reaches before becoming star forming. We define an accretion event as *hot mode accretion* if $\log(T_{\rm max}) > 5.5$ or *cold mode accretion* otherwise. Both of these accretion modes are also referred to as *pristine gas accretion*. On the other hand, if a particle is launched as a wind and subsequently re-accretes into a galaxy, we define this accretion as *wind recycling*. Unlike in our previous work, we reset $T_{\rm max}$ to 0 once a particle is launched as a wind so that at the time it recycles, it will have a different $T_{\rm max}$. In this way, we can further divide wind recycling events into *hot wind accretion* and *cold wind accretion* based on the same temperature criteria. In addition, once a gas particle spawns or turns into a star particle, we associate this star-forming event with the last accretion event of that SPH particle. Therefore, for each star particle in the simulation we can tell when, where, and in which mode its progenitor gas particle accretes. In the following sections, we will study the formation history of galaxies by looking at their star particles.

5.2 The stellar mass–halo mass functions

The stellar mass–halo mass function (SMHM) complements the GSMFs by showing how efficiently baryons turn into stars in haloes of different masses. Instead of directly plotting the ratio of stellar

[3] See Section 3 for the definition of star-forming particles in our simulations.

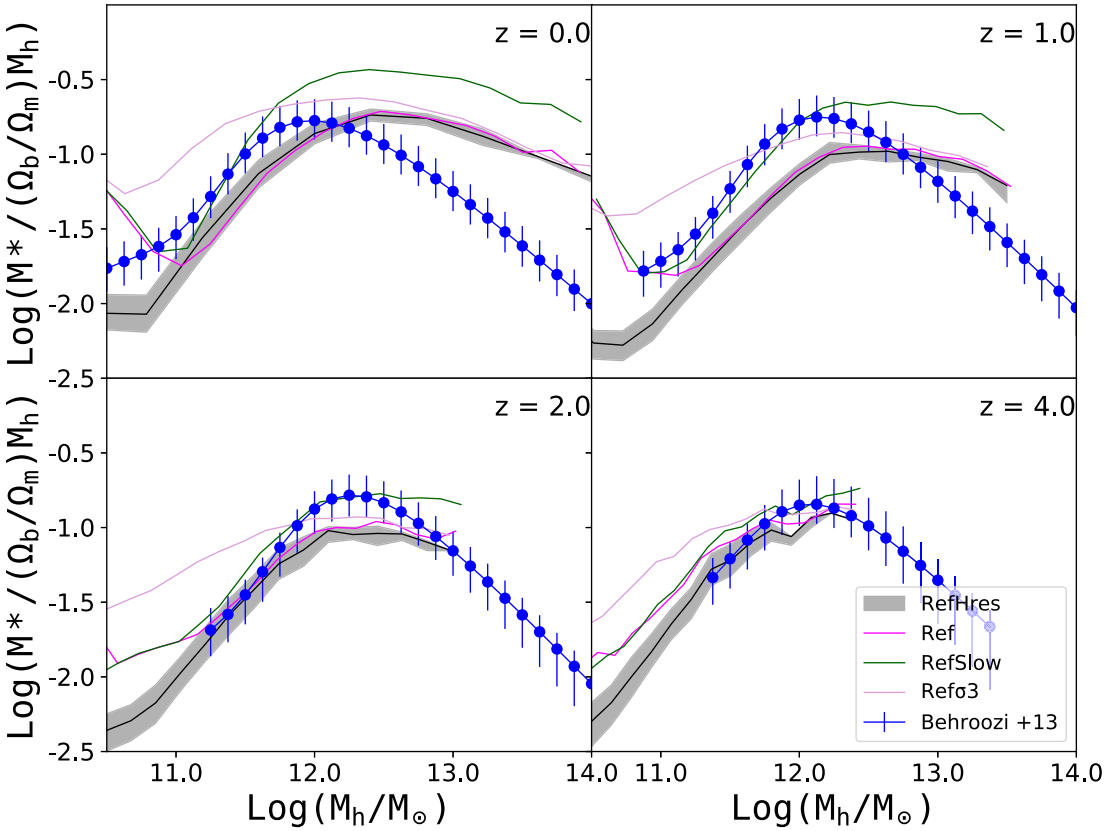

Figure 8. The stellar mass–halo mass functions (SMHMs) at $z = 0$, 1, 2, and 4. We compare the SMHMs from the same set of simulations as in Fig. 3. The solid lines are the running medians of the relation. We also show the scatter of the relation for the RefHres simulation as shaded regions that enclose 68 per cent of all galaxies within each $M_{\rm h}$ bin. The upturn in the SMHMs below $M_{\rm h} < 10^{11}$ M$_\odot$ at $z = 0$ and 1 is a selection effect owing to an artificial stellar mass cut for underresolved galaxies. The blue lines show the empirical best-fitting models from Behroozi et al. (2013) as observational constraints.

mass to halo mass, in Fig. 8 we instead plot the baryon conversion efficiency, i.e. $\epsilon_{\rm b} \equiv M_*/M_{\rm h}(\Omega_{\rm b}/\Omega_{\rm m})^{-1}$ to visually capture the small differences between the models more easily. Observationally, one determines this relation using empirical models that connect observed galaxies to dark matter haloes from N-body simulations. The empirically constrained SMHMs depend on the method used, but overall they agree with each other fairly well [see Moster, Naab & White (2018), for a recent compilation]. In Fig. 15, we compare the $z = 0$ SMHMs for the central galaxies from our simulations to the SMHM that is obtained in Behroozi et al. (2013) using subhalo abundance matching.

The Ref and RefHres simulations agree reasonably well with the observationally inferred (Behroozi et al. 2013) SMHM up to the peak at $\log(M_{\rm vir}) \sim 12$, with the largest difference at $z = 1$. The 288^3 and 576^3 simulations of this model predict similar results for $\log(M_{\rm vir}) > 11.2$, but the lower resolution simulation artificially boosts $M_*/M_{\rm h}$ at lower masses. The turnover of the SMHM is much sharper in the observations than in any of the simulations, and all models drastically overpredict $M_*/M_{\rm h}$ for $\log(M_{\rm vir}) > 13$ at $z = 0$. The Refσ3 simulation, with weaker outflows in low-mass haloes, overpredicts the observed $M_*/M_{\rm h}$ in low-mass haloes with $\log(M_{\rm vir}) < 11.5$ at all redshifts and converges to the Ref model at high masses. The RefSlow simulation, with lower wind velocities, makes similar predictions to the Ref model at $z = 4$, but at $z = 2$, and increasingly at lower redshifts, it predicts higher $M_*/M_{\rm h}$ in haloes near or above the SMHM turnover. The agreements and disagreements in Fig. 8 closely track those seen previously in the GSMF (Fig. 3).

We now examine the contributions to galaxy stellar masses in more detail, focusing first on $z = 2$ and then on $z = 0$.

5.3 Galaxies at redshift $z = 2$

Fig. 9 shows the contribution of cold, hot, cold wind, and hot wind accretion to the stellar mass content of galaxies at $z = 2$ in the Ref, RefSlow, and Refσ3 simulations. The qualitative trends are similar between the simulations. Cold mode accretion dominates, contributing to nearly 100 per cent of all star formation in small haloes with $\log(M_{\rm vir}) < 11.0$ and over half of all stars in the most massive haloes. The hot mode fraction grows with halo mass and becomes comparable to the cold mode in the most massive haloes. Wind recycling is not yet important at $z = 2$, especially in less massive haloes where most winds are able to escape the halo potential and not return.

Comparing the dotted lines and the solid lines shows the effect of changing the mass-loading factor. The Refσ3 simulation has a smaller η in low-mass galaxies compared to the fiducial simulation and, therefore, allows more gas to turn into stars. As a result, there is much more stellar mass formed from cold accretion in these galaxies, while in the other two simulations this gas is more likely to be launched as a wind before forming stars. These simulations have the same η values in massive haloes, and the stellar mass production converges at $\log(M_{\rm vir}) > 12$. This convergence implies that the winds from low-mass galaxies are not affecting the pristine gas accretion into high-mass galaxies. In principle, one expects

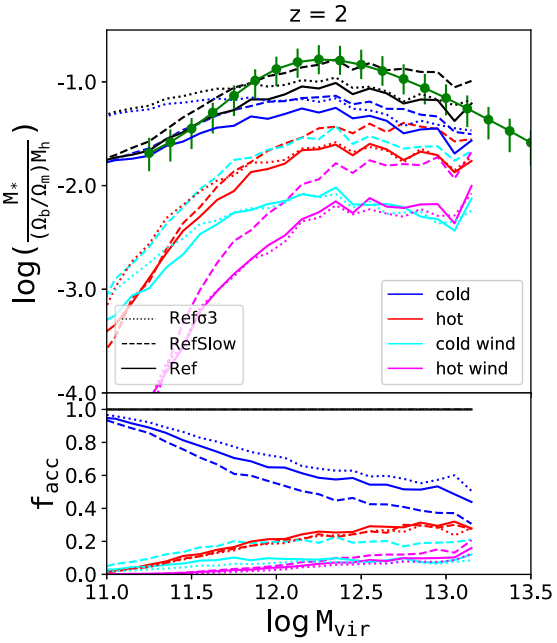

Figure 9. A closer look into the SMHM at $z = 2$. *Upper panel:* The black lines show the total mass of stars, averaged over all central galaxies from each halo mass bin, as a function of the halo mass, i.e. SMHM. The stellar masses are further divided into four categories, based on the accretion histories of their progenitor gas particle. The blue, red, cyan, and magenta lines show stellar mass formed from cold, hot, cold wind, and hot wind accretion, respectively. We also plot the empirically determined relation between stellar mass and halo masses from Behroozi et al. (2013) as the green line. *Lower panel*: The fraction of stellar mass that falls into each category. In each panel, the line styles indicate the three simulations used in this comparison.

the Ref simulation to have more wind recycling than the Refσ3 simulation owing to the larger amount of wind ejection, but this is not seen because the ejected particles have not yet had enough time to recycle. Hence, wind recycling remains a small fraction up to $z = 2$ in both models.

Comparing the dashed lines and the solid lines shows the effect of changing the wind speed. The most significant effect is that the slower winds in the RefSlow simulation result in much more wind recycling, especially the cold wind accretion in haloes of all sizes at $z = 2$. This is a direct consequence of the shorter recycling time. Another clear effect is that the fiducial simulation has less cold and hot accretion than the RefSlow simulation, indicating that the fast wind speed not only suppresses wind recycling but also plays a role in preventing pristine accretion through hydrodynamic interactions with the fresh, in-falling gas. Since these two simulations have the same outflow rate for a given halo mass, the higher stellar mass in the RefSlow galaxies can be explained by the enhanced accretion rate owing to the slow wind speed.

In summary, two major factors contribute to the different $z = 2$ SMHMs from our test simulations. The mass-loading factor controls the amount of outflow for a given halo but has little effect on the total amount of cold or hot accretion, which dominates at that redshift and above. The wind speed affects the amount of inflow. Faster winds reduce cold and hot accretion and also reduce the wind recycling by a similar amount.

5.4 Galaxies at redshift $z = 0$

The observed SMHMs at $z = 0$ show a characteristic Λ-shape with the intermediate-mass haloes [$\log(M_{\rm vir}) \sim 12$] having the peak baryonic conversion efficiency. The efficiency declines in more massive haloes as well as in less massive ones, although the reasons are likely very different: theoretical models of galaxy formation suggest that the formation of massive galaxies is characterized by the late assembly of smaller systems that formed at early times and by having little *in situ* star formation at low redshifts. On the other hand, the low-mass haloes in the local Universe followed more linear growth histories and formed many of their stars more recently. As shown in Fig. 8, our simulations in general fail to match the observed SMHMs at $z = 0$ over the entire mass range. The discrepancies are most prominent in the most massive haloes, motivating us to perform separate analyses on galaxies that form in haloes of different masses. Here we select haloes from three different mass bins and study the formation histories of their central galaxies. The low-mass bin consists of ~2000 haloes with $11.0 < \log(M_{\rm vir}) < 11.5$. The intermediate-mass bin consists of ~400 haloes with $11.85 < \log(M_{\rm vir}) < 12.15$ and the massive bin consists of ~60 haloes with $12.85 < \log(M_{\rm vir}) < 13.15$. The exact number of haloes within each mass bin varies slightly among the simulations, but we focus on comparing the average baryonic conversion efficiency, which is normalized by the total virial mass of all haloes within each mass bin.

In Figs 10 and 11, we show how stellar mass grows with time in haloes selected from the three mass regimes and divide the stellar mass at any time into categories based on their accretion histories as in the previous section.

Low-mass haloes: The stellar mass from the Ref and RefSlow simulations matches the observed value at $z = 0$, but the Refσ3 simulation overproduces stellar mass by 0.6 dex. At $z = 0$, cold accretion and cold wind recycling each contributes roughly half of the total stars formed, while hot mode accretion contributes ~10–15 per cent of star formation. Cold accretion dominates the supply of star-forming gas in all three simulations until $z = 2.0$, after which cold wind recycling and hot mode accretion start to be important. Compared to the other simulations, the haloes in Refσ3 form many more stars from both cold accretion and wind recycling, not because of more inflow but because they have less outflow as a result of the smaller mass-loading factors. The slower wind speed in the RefSlow model increases cold wind recycling by a large amount compared to the fiducial simulation. As a result, the galaxies at $z = 0$ are slightly more massive as wind recycling gains importance after $z = 2$, but their stellar masses are still consistent with the observations.

Intermediate-mass haloes: The $z = 0$ stellar mass from all three simulations is consistent with the observations within a small factor. The evolution of stellar content in these haloes is qualitatively similar to the small-mass haloes but with several major differences. First, stars from all accretion channels formed earlier in these more massive haloes, as is expected from the hierarchical assembly of galaxies. Secondly, both hot accretion and hot wind recycling, though still subdominant over most of the time, become more important at low redshifts, and together contribute ~30 per cent of the total stars formed at $z = 0$. Thirdly, cold accretion still dominates star formation at $z > 2$ but nearly stops after $z = 2$ when the shock-heated gas starts to develop a hot corona in these haloes. In the end, cold accretion only accounts for ~20 per cent of the total stars formed. Cold wind recycling still plays a critical role in determining the final stellar mass of the galaxies, and largely accounts for the

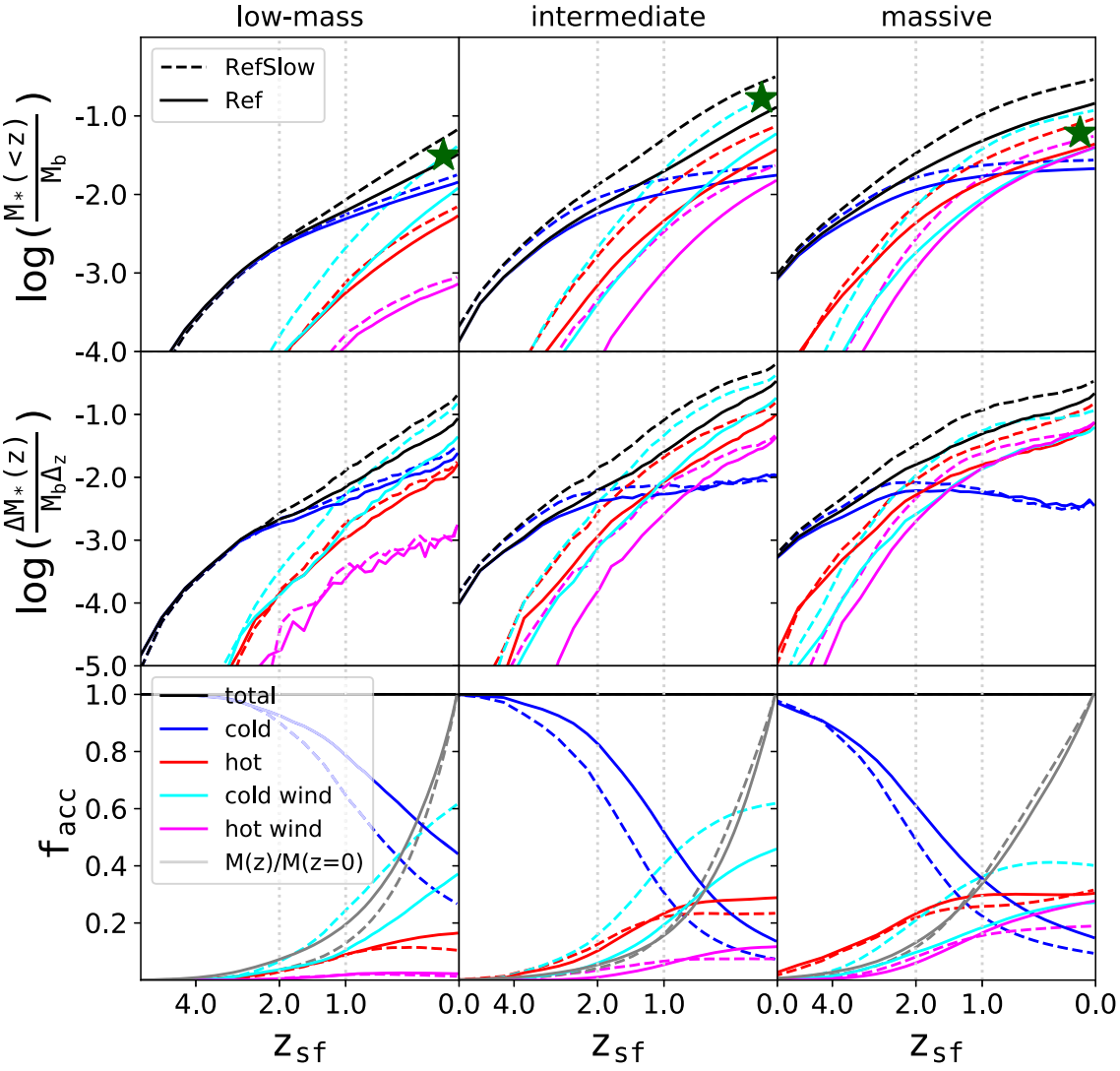

Figure 10. We select and divide $z = 0$ central galaxies into three groups based on their halo virial mass. Columns from *left* to *right* show how stellar mass on average grows with time in *low-mass* [$11.0 < \log(M_{\rm vir}) < 11.5$], *intermediate-mass* [$11.85 < \log(M_{\rm vir}) < 12.15$], and *massive* [$12.85 < \log(M_{\rm vir}) < 13.15$] haloes. Similar to Fig. 9, at each redshift, we divide star particles in these galaxies into four channels based on their accretion history: The blue, red, cyan, and magenta lines indicate cold, hot, cold wind, and hot wind accretion, respectively. The *top row* shows the cumulative mass growth history. The *middle row* shows differential stellar mass growth within a constant redshift interval Δ_z. In the upper and middle rows, we have normalized the stellar mass by the halo mass to indicate the baryon conversion factor. The green stars are the empirical results from Moster et al. (2018) for comparison. The *bottom row* shows the fraction of stars formed within each subcategory, with the grey line showing the fraction of total stellar mass at $z = 0$ that has already formed at a certain redshift. In each panel, we compare two simulations: the Ref and RefSlow simulations, indicated by the solid and dashed lines, respectively.

differences among the three simulations. Its contribution is more prominent in the RefSlow simulation.

Massive haloes: At the massive end, galaxies from the Ref and Refσ3 simulations evolve very similarly and overproduce stars by a factor of 3 at $z = 0$ (Fig. 11). The Ref simulation has larger η in small haloes, but the differences in η decrease with σ and become the same when $\sigma > 106\,{\rm km\,s^{-1}}$. Therefore, the larger mass-loading factor in the Ref simulation only affects the progenitor galaxies during the earliest stages of their assembly when they were still small. Since these haloes assembled fast at high redshifts, the different scalings of η and σ in the low-mass haloes have little effect on the massive galaxies in our simulations. Compared to the intermediate-mass haloes, they have even earlier star formation and a higher fraction of hot accretion and hot wind recycling. Except for the RefSlow simulation, where cold wind recycling is clearly more important for stellar growth than the other channels, all four accretion channels contribute comparable amounts in the other simulations, with cold accretion + cold wind recycling and hot accretion + hot wind recycling each responsible for half of the stars formed. The RefSlow simulation overproduces stellar mass by a factor of 5, more than the other simulations. Fig. 10 shows that this owes not only to more cold wind recycling because of the slower wind speed, but also because of a significantly higher amount of hot accretion and hot wind recycling than the other simulations. Furthermore, hot accretion and hot wind recycling are also higher in the low-mass and intermediate-mass regimes, but unlike in the massive haloes, they are always subdominant to the total mass budget in less massive haloes. Naturally, any feedback mechanism designed to suppress star formation at these masses would strongly impact these trends.

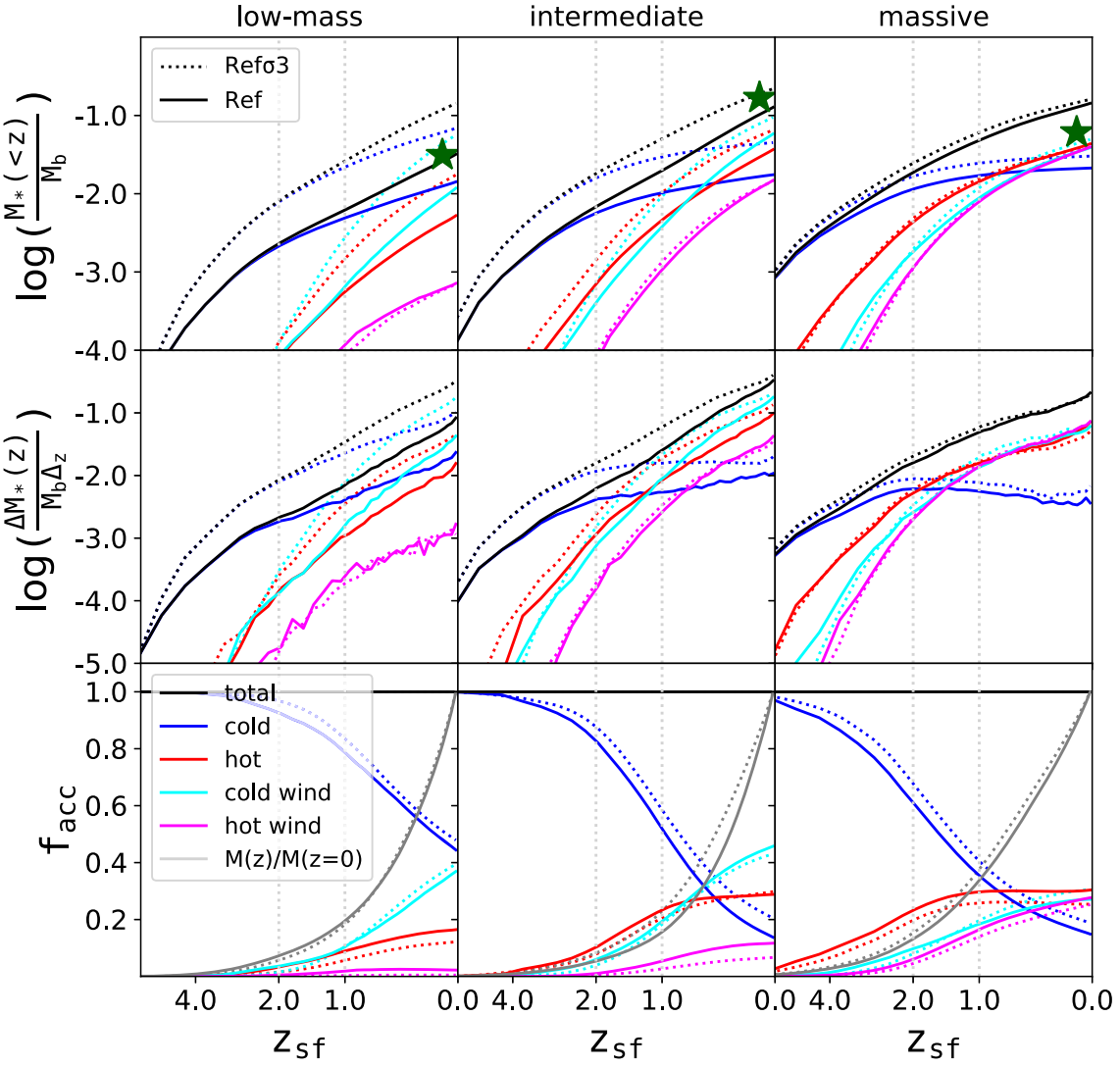

Figure 11. Same as Fig. 10, except that here we compare the Ref and Refσ3 simulations, indicated by the solid and dotted lines, respectively.

5.5 The importance of mergers

In the above discussions, we focused on studying the histories of star particles that end up in certain galaxies at a certain redshift. However, galaxies in a hierarchical Universe are often the result of many merging events. In particular, massive galaxies are often assembled from many smaller galaxies that formed in a wide range of haloes and environments. Since the *in situ* star formation efficiency, which is regulated by feedback, strongly depends on the halo mass, the final mass of a galaxy could be sensitive to feedback in those haloes where star formation was most efficient. Therefore, to understand how the feedback algorithms affect the final stellar mass of massive galaxies at $z = 0$, it is necessary to study when and where their progenitors formed.

To evaluate the importance of mergers, we need to trace the evolution of galaxies in our simulations over time. At each output, if most stars within a galaxy are found in some galaxy at the next output, we define the first galaxy as a progenitor of the second galaxy. A galaxy could have more than one progenitor at any time, and we define its main progenitor as the most massive progenitor. We consider any other progenitor of this galaxy as a merger into this galaxy between the two outputs. Therefore, we can define the main evolutionary path of a galaxy at $z = 0$ by sequentially tracking its main progenitors over time. At any time when a merger occurs, we calculate the mass ratio between the two galaxies. In this work, we define major mergers as those that involve two galaxies with a mass ratio over 1/5. One caveat is that some galaxies take longer than a few outputs to completely merge with their host galaxies. In some situations, they were first grouped with the host galaxy during the first pass-by but left and became a separate galaxy later on, before they finally merged again. To avoid counting these galaxies as individual mergers multiple times, we consider only the first merging event by requiring that the mass of the host galaxy be at its maximum up to the merging event. Therefore, if the merging galaxy later left, the mass of the host galaxy would decrease and any subsequent pass-by will not be counted until the merger is complete. This criterion effectively removes most of the spurious mergers without missing any real mergers.

To evaluate the importance of mergers, we look at galaxies at $z = 0$ and determine what fraction of stars each galaxy accreted through major mergers and where and when the stars present at $z = 0$ form. Fig. 12 shows that for most galaxies, the fraction of stars acquired through major mergers is less than 10 per cent. In general,

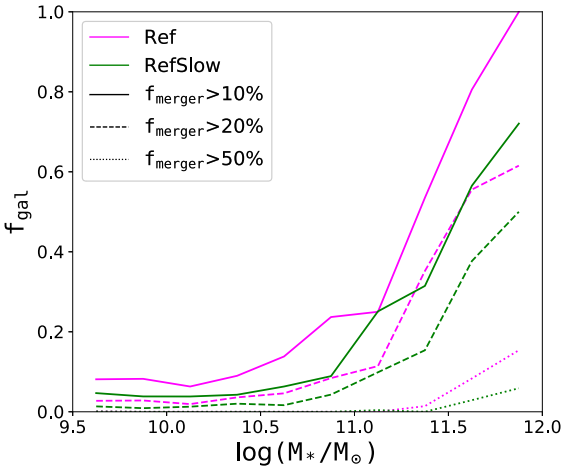

Figure 12. The dotted, dashed, and solid lines indicate the fraction of galaxies that have more than 10, 20, and 50 per cent of their $z = 0$ stellar mass gained by major mergers. The Ref and RefSlow simulations are shown in magenta and green, respectively. In general, the importance of mergers increases with M_*, but even in the most massive galaxies, the fraction of stars from mergers are less than those formed *in situ*.

more massive galaxies have a higher fraction of their stars formed in other galaxies and merged with it at later times, but even in the most massive bins, only 30 per cent of galaxies have more than half of their stars added through major mergers. The major merger fractions are also similar between the Ref and RefSlow simulations. Galaxies in the RefSlow simulation in general have a higher fraction of stars formed *in situ* because of more wind recycling on to the main progenitors. These results do not change very much if we include mergers with a mass ratio less than 1/5.

In summary, the stellar growth of galaxies in our simulations is dominated by *in situ* star formation, with major mergers contributing a small fraction, except in the most massive galaxies. The final stellar mass of a galaxy is in most cases determined by the growth of its most massive progenitor, which is in turn regulated by how efficiently feedback suppresses star formation during the entire time of the evolution of the progenitor and its host halo. However, the relative importance of mergers in galaxy growth could increase if one added additional feedback to remove all the late-time star formation in massive galaxies, as required to match observations.

5.6 Wind recycling

Wind recycling dominates the supply of star-forming gas at lower redshifts and is responsible for a considerable fraction of the total stellar mass in most haloes. In this section, we will show that wind speed strongly affects the recycling time-scale $t_{\rm rec}$ of the launched winds.

The amount of winds that re-accrete after being launched is closely related to the recycling time-scale $t_{\rm rec}$ (Oppenheimer et al. 2010), defined as the time between a particle being launched as wind and it becoming star forming again. Fig. 13 compares the $t_{\rm rec}$ of wind particles from the three simulations with different wind speeds (see Fig. 2). The wind particles from the ezw simulation have $t_{\rm rec}$ that strongly depends on the halo mass. The deep gravitational potential of massive haloes causes wind particles to fall back shortly after being launched, creating a galactic fountain that is categorically different from the galactic scale winds in smaller galaxies. Oppenheimer et al. (2010) use the same wind algorithm in their simulations and find a similar trend. They refer to it as 'differential recycling', which is key to regulating star formation as a function of halo mass and thereby shaping the GSMFs. However, the recycling times from Oppenheimer et al. (2010) are greatly affected by the fact that their wind speeds do not scale as $v_{\rm w} \propto \sigma$ after they leave the galaxy (Fig. 2) as they were originally intended, which was the motivation for our new wind model.

The other two simulations have a mass-dependent enhancement to the wind speed. Increasing wind speed with mass has a direct effect on $t_{\rm rec}$, with a stronger enhancement (Ref) leading to a longer $t_{\rm rec}$ in massive haloes. Similar to what Fig. 2 indicates, the wind dynamics inside these haloes are sensitive to their initial speed. For example, in the most massive galaxies at $z = 2$, the average wind speed in the Ref simulation is ∼2 times faster than in the RefSlow simulation while the recycling time is ∼3 times longer.

We have further divided wind recycling into cold wind and hot wind recycling based on whether or not the wind particle heats up to $10^{5.5}$ K. In the middle row of Fig. 13, the dotted lines show that the hot winds are less likely to re-accrete into galaxies by $z = 0$ than cold winds. For the winds that did recycle, the upper rows of Fig. 13 show that the recycling time-scales are significantly longer for the hot winds (dotted) on average. Most cold winds that formed stars at $z \sim 0$ were launched well below $z = 1$, while most hot winds were launched around $z = 2$. Moreover, Figs 10 and 11 show that even though hot wind recycling is nearly negligible in low-mass and intermediate-mass haloes, it is important to the late star formation in massive galaxies. Because of the long $t_{\rm rec}$ of hot winds, it also indicates that a considerable fraction of stars in massive galaxies formed from outflow material launched long ago, at least in our simulations.

The wind particles in our simulations are shock heated immediately after they hydrodynamically recouple to the ambient SPH particles. The initial wind speed plays a critical role in determining the post-shock temperature of the wind particles. Once they heat up to a temperature where cooling becomes inefficient, they will likely stay hot and become indistinguishable from a normal gas particle of the hot corona gas. The evolution of the hot wind particles thus depends more on the cooling physics than the dynamics that governs the recycling of cold wind particles. The bottom row of Fig. 13 shows that the fraction of winds that became hot is very sensitive to wind speed. The hot wind fraction is significantly higher in the Ref simulation, where wind heating is more efficient owing to the faster wind speeds. Note that with a sufficiently fast wind speed, our wind algorithm naturally results in a multiphase outflow, without the need to artificially add a hot component to the winds at launch as in MUFASA (Davé et al. 2016). We also find that the hot wind fraction is negligible in even the most massive galaxies in the ezw simulation, where the wind speeds are even lower. This was the wind model used in Davé et al. (2013).

However, we must caution that the interactions between the winds and the halo gas likely involve processes such as hydrodynamic instabilities and thermal conduction that are unresolved in our simulations and likely even in galaxy zoom-in simulations with the highest resolution today (e.g. Schneider & Robertson 2017). The evolution of winds inside and outside galactic haloes in galaxy simulations, therefore, likely depends as much on numerics as on the true underlying physics. Hence, the behaviour and the effects of wind recycling must be re-examined with future simulations that have higher resolution or accurate and numerically robust subgrid models that incorporate necessary physics that has been neglected or incorrectly modelled in simulations up until now. Simulations that concentrate resolution in gaseous haloes (Hummels et al. 2019;

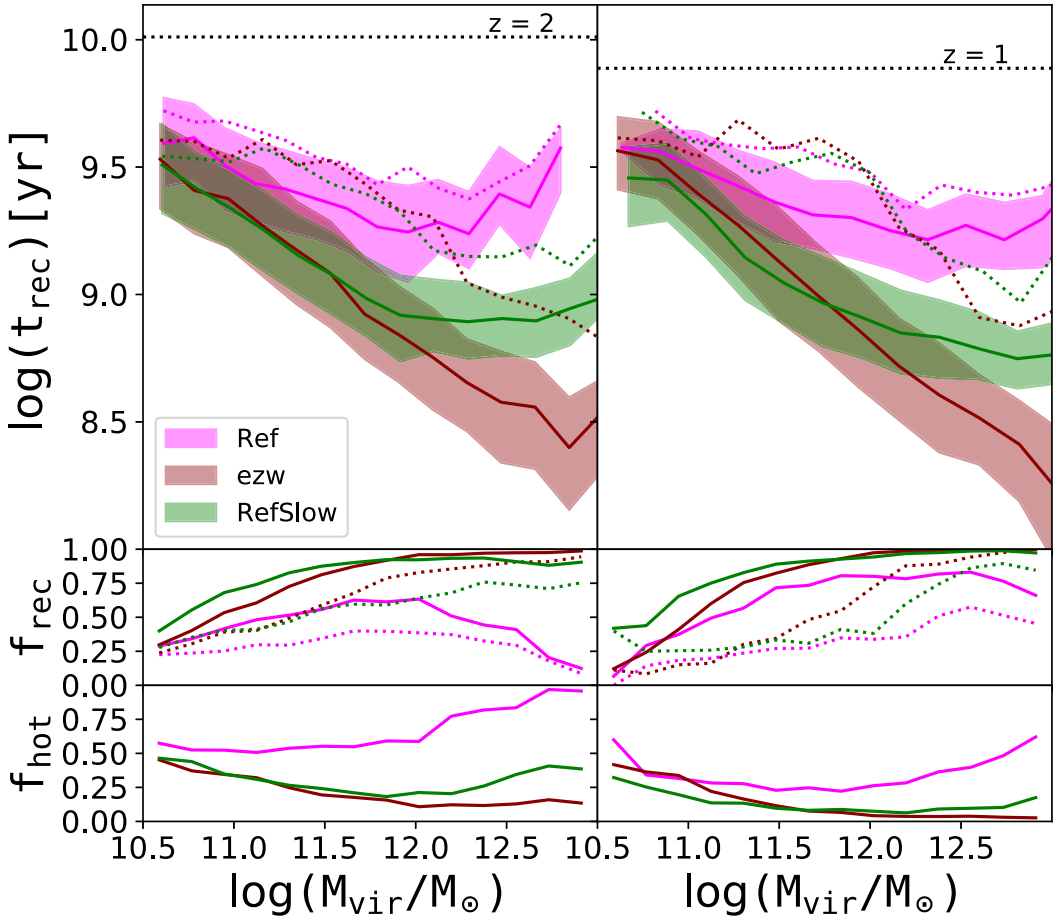

Figure 13. *Upper panels*: The median recycling time $t_{\rm rec}$ of winds that have recycled by $z = 0$ as a function of the virial mass $M_{\rm vir}$ of the halo from which the winds were launched. We only include winds launched from central galaxies. The dotted lines show $t_{\rm rec}$ only for winds that become hot. The *left-* and *right-hand* panels show results for winds launched at $z = 2$ and 1, respectively. We include all wind particles that are launched during a small redshift window with $\Delta_z = 0.002$ at these redshifts. The dotted horizontal line in each panel indicates the lookback time at that redshift and is the upper limit of $t_{\rm rec}$ for those winds. The shaded area shows the 1σ scatter in each $M_{\rm h}$ bin. *Middle panels*: The solid lines indicate the fraction of all winds that have ever re-accreted on to any galaxy at least once by $z = 0$. The dotted lines include only those winds that become hot. In general, the fraction of hot winds that recycle is lower. *Bottom panels*: The fraction of all winds that become hot, regardless of whether or not they have recycled by $z = 0$.

Peeples et al. 2019; van de Voort et al. 2019) can improve modelling of physics in the CGM, though even with this approach the resolution may not be sufficient to accurately model interactions within the multiphase CGM (Scannapieco & Brüggen 2015; Schneider & Robertson 2017) and in addition it may be difficult to quantify recycling for ensembles of galaxies with a range of properties.

5.7 Implications for additional feedback

Feedback processes are essential in cosmological simulations to successfully reproduce the observed stellar content of the Universe. Stellar feedback such as galactic winds generated from the brightest stars and SNe has been widely applied to explain the growth of small galaxies, but these processes alone are usually insufficient to suppress the growth of massive galaxies. The stellar feedback models in simulations are usually tuned to match observational constraints at the low-mass end, while one often invokes additional feedback such as AGN feedback to produce more realistic massive galaxies. It is also unclear what exact role AGN feedback plays in suppressing star formation. It could work as preventative feedback that limits the amount of inflow, or as kinetic feedback that drives additional outflows from galaxies. In the previous sections, we have shown that changing the parameters of our particular stellar feedback model within our explored range could significantly affect galaxy growth, even in the most massive haloes. This hints at the possibility that a combination of carefully tuned galactic wind parameters might be able to simultaneously reproduce the stellar content on all mass scales at any redshift. Even if the wind model is unable to meet all the constraints, it is important to understand the shortcomings of the current model that have to be solved with additional feedback processes.

A successful galaxy formation model that reproduces $z = 0$ results must also be able to match observations from higher redshifts. At $z = 2$, we have shown that a strong halo mass dependence of the mass-loading factor is key to matching the faint-end slope of the SMHM, while different wind speeds are responsible for variations of the stellar mass in massive haloes. The Ref and RefSlow simulations both reasonably match the observed relation at $z = 2$. The RefSlow simulation produces more stars in intermediate to massive haloes owing to slower winds and a short recycling time, and agrees better with observations at the 'knee' but worse at the massive end.

At $z = 0$, the discrepancy at the massive end grows, resulting in a factor of 3 times more stars in the massive bin and even larger discrepancies in more massive haloes. The grey lines in the bottom panels of Figs 10 and 11 show the build-up of stars that end up in the massive galaxies. They are consistent among the simulations, with more than 80 per cent of stars formed after $z = 2$ and 60 per cent of stars formed after $z = 1$. Therefore, in our simulations it is the late star formation in massive galaxies that must be greatly reduced to match the $z = 0$ observations. Section 5.5 confirms that most of these stars formed *in situ* instead of through merging. A successful model must maintain the level of star formation up to $z = 2$ as in the RefSlow simulation but significantly reduce the amount of stars formed afterwards. In fact, the top right panels of Figs 10 and 11 show that galaxies in the massive bin have already formed by $z = 2$ as many stars as required to match the $z = 0$ observations. Hence, to make these galaxies agree with the $z = 0$ constraint, nearly all *in situ* and *ex situ* star formation after $z = 2$ needs to be suppressed. Observationally, this phenomenon is known as downsizing, i.e., massive galaxies at $z = 0$ formed earlier but have little late-time star formation. However, it is challenging to reproduce this effect in our simulations without additional feedback.

Stars from cold accretion mostly formed at high redshifts in small haloes that later assembled into the massive galaxies. The most efficient way to remove them from our simulations is to have stronger winds, i.e. stronger mass-loading factors in those haloes. However, having too much winds early will unavoidably fail to match observations at higher redshifts. The right-hand panels of Figs 10 and 11 show that cold accretion has nearly stopped after $z = 2$ for these galaxies but hot accretion and wind recycling continue growing rapidly at low redshifts, and is responsible for most of the excess stars formed. After $z = 2$, the stars in massive galaxies that must be prevented from forming come from almost equal parts: hot accretion, hot wind re-accretion, and cold wind re-accretion. Hence, preventing hot gas from cooling and forming stars at these times will eliminate both the hot mode accretion and hot wind re-accretion and will lessen the tension in massive haloes. There are several potential mechanisms, such as AGN and cosmic ray heating, that could reduce the amount of this cooling gas but they are not yet included in our simulations. The hot wind recycling would be harder to affect by extra heating, because the higher metallicity of this gas makes it cool faster. In hydrodynamic simulations, mixing between ejected wind elements and the surrounding gas may have a large impact on the amounts of hot and hot wind accretion. It is, however, unclear whether this type of feedback could prevent the $\sim$1/3 of stars formed through cold wind re-accretion after $z = 2$ from forming, which is also necessary to match the observations. It is possible that a more accurate treatment of the cloud-CGM interaction would allow a larger fraction of these winds to become hot, alleviating this problem.

6 THE HIGH-RESOLUTION SIMULATION OF THE REFERENCE MODEL

In this section, we present key results from the high-resolution RefHres simulation. It adopts the new wind launch algorithm as described in the previous sections using our fiducial set of wind parameters listed in Table 1. It is also implemented with the numerical improvements to the SPH hydrodynamics introduced by Huang et al. (2019). We will focus on those predictions that have changed significantly from Huang et al. (2019) and from our previously published work with our new wind algorithm.

6.1 The stellar content

Fig. 14 shows that the GSMFs from our fiducial simulation, shown as black lines in each panel, are mostly consistent with observations at all redshifts from $z = 0$ to 4. The agreement is particularly good at the faint end except for $z = 0$, where our simulation slightly underproduces the number of these low-mass galaxies. At the massive end, our GSMFs agree with observations at $z = 1$ and 4. However, our fiducial simulation produces too many massive galaxies at $z = 0$ and too few massive galaxies at $z = 2$, even after taking account for systematic uncertainties in the stellar mass measurements at these redshifts.

The level of our agreement is comparable to other cosmological hydrodynamic simulations such as EAGLE (Furlong et al. 2015), MUFASA (Davé et al. 2016), and illustrisTNG (Pillepich et al. 2018b), except for massive galaxies at $z = 0$ where AGN feedback incorporated in these other simulations more strongly suppresses stellar mass growth. The *ezw* model as implemented by Davé et al. (2013) includes an ad hoc quenching scheme in massive galaxies to reproduce the $z = 0$ GSMF. Without this quenching scheme, however, the *ezw* wind formulation produces worse agreement with observations: too many small galaxies at higher redshifts ($z = 2$ and 4) and too many massive galaxies at lower redshifts ($z = 1$ and 0). We have shown in Section 4 that the success of reproducing the faint end of GSMFs at $z > 1$ relies on a steeper scaling between the mass-loading factor η and the halo mass. On the other hand, suppressing the growth of massive galaxies relies on a higher wind velocity to effectively remove cold gas from the galaxies.

Fig. 14 also shows that different hydrodynamic algorithms (comparing ezwDESPH and ezw) have noticeable effects on the GSMFs, principally at the massive end, although these are much less significant than the changes driven by the wind algorithm. Comparing the Ref simulation and the RefHres simulation shows that the results are also robust to numerical resolution, but note that in the higher resolution simulation we have increased the overall wind speed by a small factor to obtain a similar v_{25}–v_c relation.

Fig. 15 shows that the baryon conversion efficiency from our fiducial simulation agrees well with observations (Behroozi et al. 2013; Moster et al. 2018) in small haloes and reaches a similar peak value, but it becomes too high in more massive haloes. This is a more clear illustration of the excess of stars in massive haloes than that seen in the $z = 0$ GSMF. Comparing to the ezw simulation, which uses the same SPH method but the *ezw* wind model, the new wind algorithm significantly reduces the stellar content in these massive galaxies but it is still not enough to match the observations. Also, increasing the numerical resolution has little effect on the SMHM.

6.2 SDE

Fig. 16 shows the SDE of a few simulations. Our fiducial simulation, shown as the thick, black line in Fig. 16, agrees with the observational data to within 0.1 dex below redshift $z = 3$. At higher redshifts, it falls in between the Muzzin et al. (2013) data and the upper limits from González et al. (2011). Our simulation is capable of capturing the general trend of the cosmic SDE. Since the stellar density at any epoch is equivalent to the integration of the GSMFs at that redshift, the success of matching the GSMFs at various redshifts is key to matching the observed SDE.

The original *ezw* model not only produces too many stars at $z \sim 0$, owing mostly to the excess of stellar mass in massive galaxies, but also has started overproducing stars since $z = 5$ owing to an

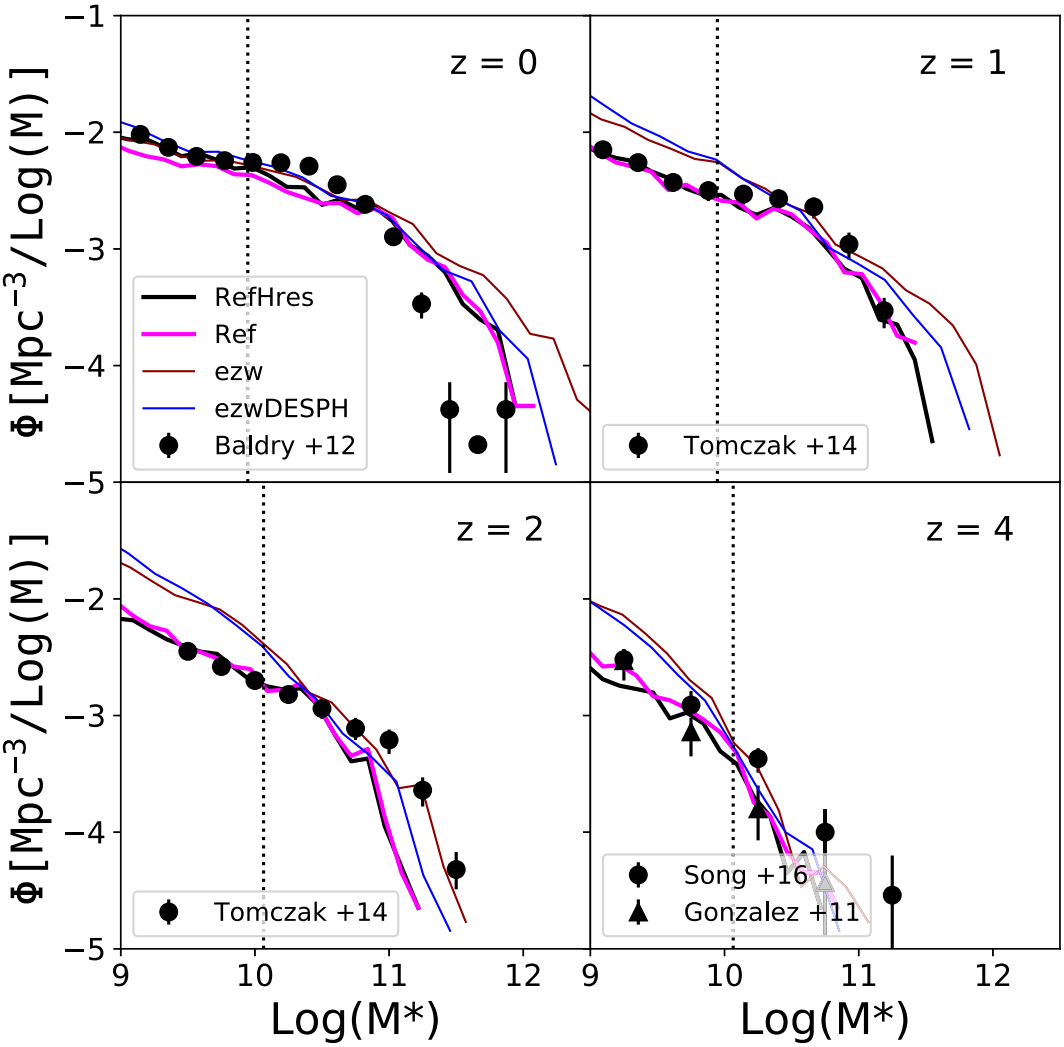

Figure 14. Same as Fig. 3, except that here we show a different set of simulations, including the fiducial high-resolution simulation RefHres. See the text and Table 1 for descriptions of these models. The vertical dotted lines correspond to the mass of 1024 SPH particles in the RefHres simulation and 128 SPH particles in the other simulations.

insufficiently large η. Changing the numerics from the ezwDESPH simulation to the ezw simulation allows more star formation at lower redshifts, but the effects are less significant than the effects of changing the wind algorithm.

6.3 Gas fractions and metallicity

Fig. 17 shows the cold gas fractions $f_{\rm gas}$ at $z = 0$ and 2 in the left-hand panels. In the simulations, we define $f_{\rm gas}$ as

$$f_{\rm gas} \equiv \frac{M_{\rm gas}}{M_{\rm gas} + M_*}, \tag{18}$$

where M_* is the total stellar mass of the galaxy, and $M_{\rm gas}$ is the total mass of the ISM gas in that galaxy. To determine which SPH particles are treated as multiphase ISM gas in our simulations, we assume a physical density threshold of $n_{\rm H} > 0.13\,{\rm cm}^{-3}$ and a temperature threshold of $\log T/{\rm K} < 4.5$. Any SPH particles within a galaxy that meets these criteria are included when calculating $M_{\rm gas}$. These sharp thresholds are somewhat arbitrary, so comparisons to observations should be interpreted with caution (Davé et al. 2011b).

At $z = 0$, we add the data from Peeples et al. (2014), which are compiled from various data sets (McGaugh 2005, 2012; Leroy et al. 2008; Saintonge et al. 2011). The data points show the averaged atomic + molecular gas fractions in each stellar mass bin, with error bars indicating the 16th and 84th percentiles, which is the same range chosen for the simulated data. Our fiducial simulation reproduces the observed trend very well, though it slightly overpredicts the cold fractions in massive galaxies.

Compared to the ezwDESPH simulation, small galaxies with $\log(M_*/{\rm M}_\odot) < 10$ in the fiducial simulation are more gas rich, making the scaling relation at the faint end agree with the observations from Peeples et al. (2014). Comparing the Ref and RefHres in the figure shows that this result is resolution independent. At the massive end, the gas fractions in the fiducial simulation are close to those from the ezwDESPH simulation. Galaxies in the ezwDESPH simulation are in general more massive than their counterparts in the fiducial simulation. Therefore, at a fixed halo mass galaxies in

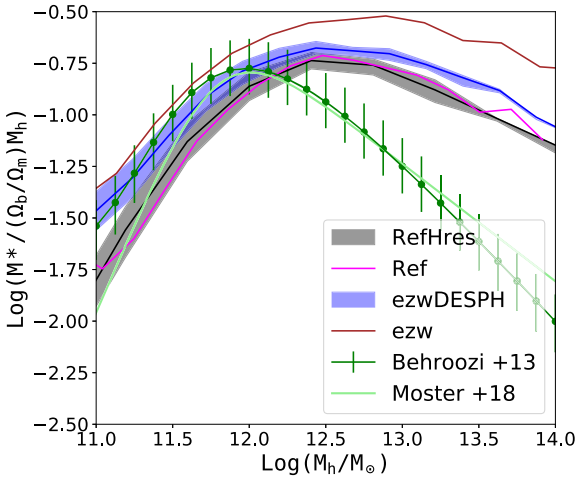

Figure 15. The stellar mass–halo mass functions at $z = 0$. We compare the SMHMs from the same set of simulations as in Fig. 14. The solid lines are the running medians of the relation. We show the scatter of the relation for the RefHres and ezwDESPH simulations as shaded regions that enclose 68 per cent of all galaxies within each M_h bin. The green lines show the empirical best-fitting model from Behroozi et al. (2013) and Moster et al. (2018) as observational constraints.

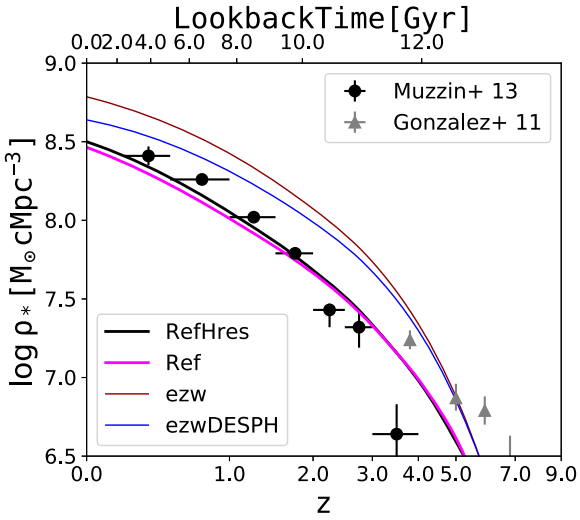

Figure 16. Same as Fig. 7, except that here we show results from the fiducial high-resolution simulation compared with a few test simulations. Our fiducial wind model (in the RefHres and Ref simulations) reproduces the observations well, but the original *ezw* wind model starts overproducing stars at very early times.

the fiducial simulation actually contain a higher gas mass. In future work, we will track gas accretion through cosmic time in detail to understand the origin of cold gas in galaxies.

At $z = 2$, a detailed comparison with observations is unavailable owing to a lack of direct measurements of the cold gas content at high redshifts. Nevertheless, it is consistent with the indirect observations (e.g. Popping et al. 2015) that the cold gas fractions are generally higher than at $z = 0$ at a fixed stellar mass. The differences between the fiducial and ezwDESPH simulations are much larger at this redshift, with much lower gas fractions in massive galaxies than in the fiducial simulation.

In the right-hand panels of Fig. 17, we compare the gas-phase MZRs from our fiducial simulation with observations. We calculate the gas-phase metallicity for each galaxy by averaging over all ISM particles within the galaxy, weighted by their SFR. We use oxygen as the metallicity tracer and adopt a solar value of $[O/H]_\odot + 12 = 8.69$ (Asplund et al. 2009). We use the Sanders et al. (2015) ($z \sim 2.3$) and Tremonti et al. (2004) data for comparisons. Since they measure metallicity using different calibrations, we convert the Sanders et al. (2015) data to the Tremonti et al. (2004) calibration using the fitting formula from Kewley & Ellison (2008). This increases the overall normalization of the Sanders et al. (2015) data by 0.1–0.3 dex.

At face value, the comparison in Fig. 17 shows a slight overproduction of gas-phase metallicity with the right overall trend at $z = 2$, but a more severe discrepancy at $z = 0$ where the simulations underpredict the metallicity of low-mass galaxies and overpredict the metallicity of high-mass galaxies. The caveat is that calibration and measurement uncertainties have a large impact on the observed mass–metallicity relation (Kewley & Ellison 2008). Furthermore, the initial mass function (IMF) averaged oxygen yield is uncertain, and it could change with galaxy mass if the IMF itself changes. In principle, the mass–metallicity relation is a strong diagnostic of outflow efficiency (Finlator & Davé 2008), and it should also be sensitive to the amount of metal recycling in winds.

6.4 Intergalactic and circumgalactic medium

Galactic winds are not only important as a feedback mechanism that suppresses galaxy growth, but are also essential to explain the enrichment of the IGM and the CGM as they carry the metals that are produced inside the galaxy into the outer halo and beyond. Measurements of the metal content in the IGM/CGM using quasar absorption spectroscopy [see Tumlinson, Peeples & Werk (2017), for a review] provide crucial constraints for cosmological simulations (Oppenheimer & Davé 2006; Oppenheimer et al. 2012; Ford et al. 2014, 2016). In this section, we show how the new wind algorithm in our fiducial simulation affects the metal distributions in the IGM/CGM.

To mimic the observational measurements, we create mock quasar absorption spectra using SPECEXBIN as in Huang et al. (2019). A more detailed description of the technique can be found in Oppenheimer & Davé (2006). In short, we generate random sightlines covering a redshift range from $z = 0$ to 0.5 through the simulation volume. On each of these long sightlines, we calculate the optical depth of multiple ions in redshift space based on the properties of the surrounding gas, such as the density, temperature, velocity, and metallicity. We use a uniform ultraviolet background (Haardt & Madau 2012) to calculate the ionization level of each ion. We normalize the strength of the background to match the Lyman α decrement measurements (Huang et al. 2019). From these mock spectra, we further obtain observational quantities such as column densities and equivalent widths for each ion by fitting their line profiles using the Voigt profile fitting software AUTOVP (Davé et al. 1997). In this paper, we generate 71 sightlines for each of the low-resolution simulations and 400 sightlines for the RefHres simulation.

Fig. 18 compares the column density distributions (CDDs) of O VI and Ne VIII from the four simulations. Comparison of ezw to ezwDESPH shows that numerics have a strong effect on the CDDs of these ions, as shown by Huang et al. (2019). The new wind model (Ref) slightly increases the number of high-column density absorbers compared to the *ezw* wind (ezw) but does not strongly affect the low-column density absorbers. The CDDs are

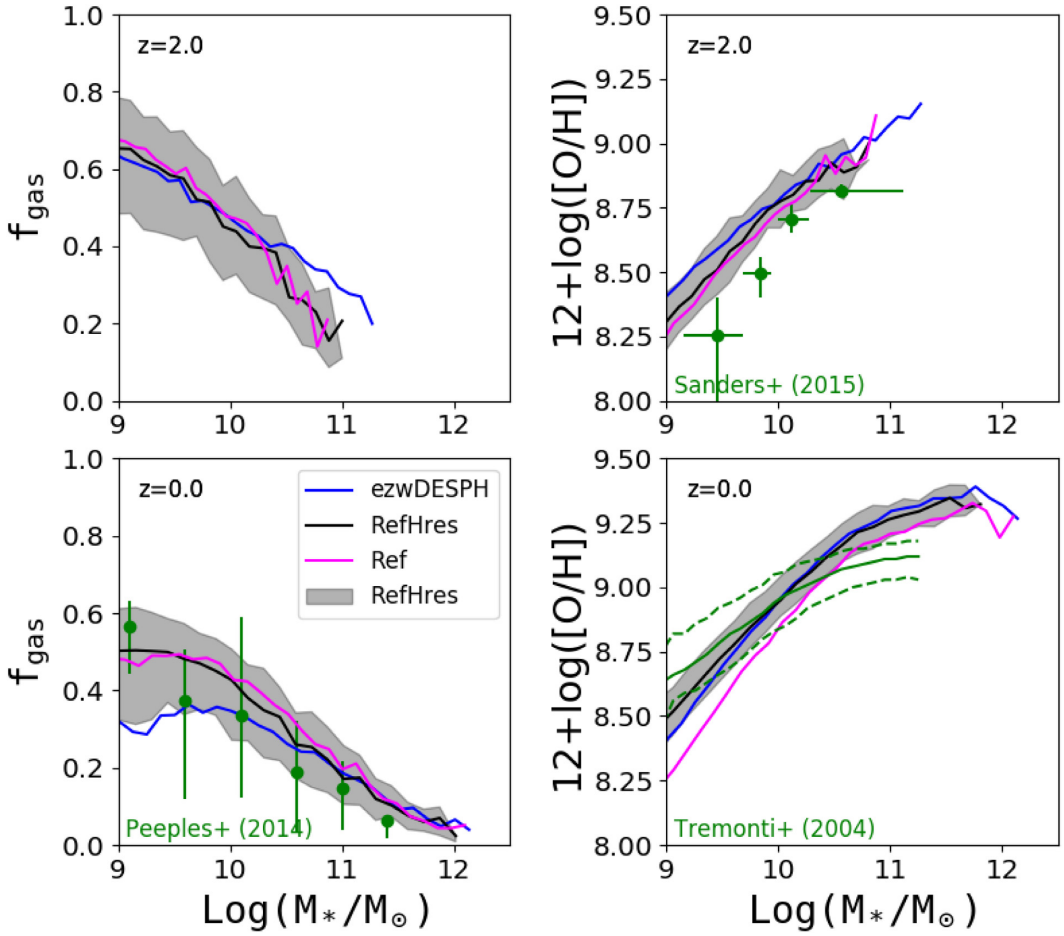

Figure 17. *Left-hand panels*: cold gas fractions (defined in the text) as a function of stellar mass at $z = 2$ (*upper panel*) and $z = 0$ (*lower panel*). The observational data in the lower panel are compiled by Peeples et al. (2014), with error bars denoting the 16–84 per cent range. *Right-hand panels*: gas-phase mass–metallicity relations at $z = 2$ (*upper panel*) and $z = 0$ (*lower panel*). The $z = 2$ data are from Sanders et al. (2015) and the $z = 0$ data are from Tremonti et al. (2004). The shaded area in each panel shows the 16–84 per cent range of the results from the fiducial high-resolution RefHres simulation. We also show the medians from the lower resolution Ref as magenta lines.

also sensitive to numerical resolution, as the higher resolution simulation RefHres has fewer absorbers than the lower resolution simulation.

The contours in Fig. 19 show how metals are distributed in the temperature–density phase space at $z = 0$ in the three simulations. Comparing the ezw (middle panels) and the ezwDESPH (left-hand panels) shows the effects of changing numerics and cooling physics on the metal distributions and the high-ion absorbers. We have studied those effects in greater detail in previous work (Huang et al. 2019). The main effect is that there are more metals in the warm–hot gas (WHIM; upper left quadrants) owing to better resolved shocks around filaments.

Comparing the RefHres simulation (right-hand panels) to the ezw simulation (middle panels) shows that the new wind algorithm spreads a considerable amount of metals into the warm–hot IGM gas and the hot, dense gas as a result of both the stronger mass loading in low-mass galaxies and the faster wind speed. Since we do not allow metal mixing between the enriched wind particles and the pristine IGM gas, the enhanced metallicity at below cosmic mean density comes directly from wind particles that escape into the IGM. The higher metallicity in the hot gas is likely because of wind particles being able to remain longer in hot haloes before re-accreting on to the galaxies.

One numerical caveat is that when the original SPECEXBIN calculates the local gas properties such as the temperature at a given location in a sightline, it averages over all neighbouring particles close to the sightline without distinguishing wind particles from normal SPH particles. This potentially leads to errors in a multiphase gas, such as when cold, metal-rich wind particles are among hot CGM particles. Therefore, we modified SPECEXBIN to take into account the contribution of each surrounding particle to the spectra on a particle-by-particle basis. However, we do not find any significant differences in the results for the high ions from using these two different methods.

7 SUMMARY

Galactic winds are crucial to galaxy formation. At present, hydrodynamic simulations that model cosmological volumes (i.e. many Mpc on a side) lack the resolution to generate winds from physical processes in the ISM. Such simulations, therefore, employ subgrid prescriptions that are designed to capture the phenomenological behaviours of these processes. In this paper, we revisit a wind implementation that is based on a numerical algorithm proposed and developed by Springel (2005), Oppenheimer & Davé (2006), and Davé et al. (2013). We take into account new constraints from

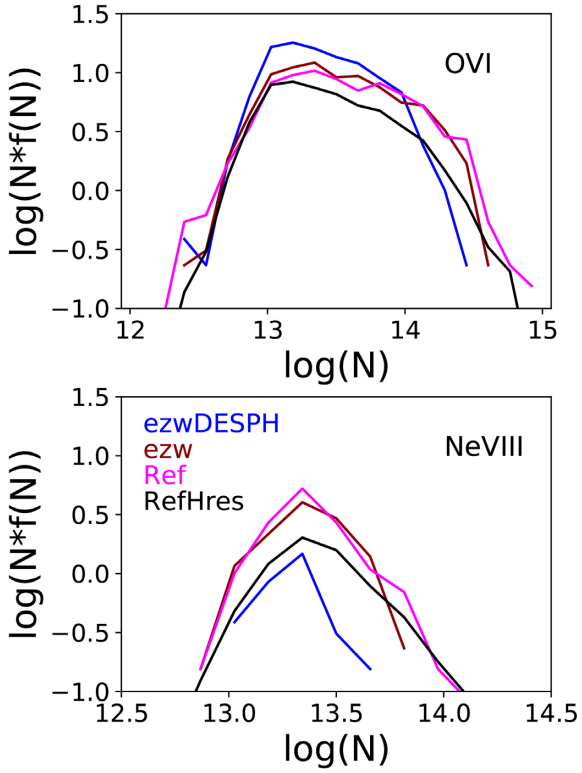

Figure 18. The CDDs of O VI (*upper panel*) and Ne VIII (*lower panel*). We obtain the statistics from random sightlines that span from $z = 0.0$ to 0.5 as described in the text. Results from the four simulations are colour coded according to Table 1.

high-resolution zoom-in simulations (M15) and statistical properties of galaxies at high redshifts, such as their stellar mass functions, and make several changes to our wind algorithm. We examine the ability of the new algorithm to reproduce a wide range of observations and study the sensitivity of these predictions to variations in model parameters.

The basic design of the wind algorithm is that in star-forming galaxies, cold and dense SPH particles are stochastically ejected from their host galaxies with an initial momentum kick to model large-scale star formation-driven winds. The mass-loading factor η determines the rate at which particles are ejected and the wind speed $v_{\rm w}$ determines the initial velocity given to the ejected particles. Observations and analytic calculations have shown that both of these parameters correlate with properties of their host galaxy or host halo such as the SFR and the characteristic velocity σ (Rupke et al. 2005), but an accurate determination of these scalings is unknown. Previous wind algorithms often parametrize them as $\eta \propto \sigma^{-1}$ or σ^{-2}, and $v_{\rm w} \propto \sigma$, following the analytic formulation for momentum-driven or energy-driven winds (Murray et al. 2005).

However, it becomes clear in cosmological simulations that artificial numerical treatments as well as fine-tuning of the model parameters are required to successfully reproduce key observables, such as the galaxy stellar mass function, owing to limitations in the numerical resolution of simulations and the simplicity of the analytic models. Furthermore, recent zoom-in galaxy simulations (e.g. M15) suggest different wind scalings than the analytic models. Most importantly, simulations necessarily impose these scalings at wind launch, while they are supposed to hold for gas that has escaped the dense ISM. When we measure the resultant wind scalings outside of galaxies, the original scalings no longer hold. We have therefore altered our wind launch algorithm to reproduce, approximately, the wind properties measured by M15 at 25 per cent of the halo virial radius.

Major updates from our previous wind algorithm include the following: (1) We allow more freedom when assigning η and $v_{\rm w}$. In particular, we allow a stronger dependence of η on σ, or equivalently, the halo mass. (2) We allow newly ejected wind particles to temporarily decouple from their host galaxies dynamically before they reach a density threshold of $0.1\rho_{\rm SF}$. The new algorithm may appear to be less deterministic than the original one by having a few more tunable parameters, but it is an unavoidable compromise to the uncertainties and limitations of our current knowledge of the nature of galactic winds. The primary focus of this paper is, therefore, not to extensively search for a set of parameters that best reproduce the observed Universe but rather to explore and characterize how some of the well-established observational results on galaxy formation could be affected by a physically plausible range of wind model parameters. Naturally, we perform this exploration within the narrow confines of our wind model. Differences between the methods used by different simulation groups in the literature could be larger.

We find that the faint-end slopes of the GSMFs at $z > 1$ in our simulations are most sensitive to the power-law index β_η, which determines how strongly the mass-loading factor η depends on σ in low-mass galaxies (Section 4.1.1). The energy-driven scaling $\eta \propto \sigma^{-2}$ that was used in our previous simulations (e.g. Davé et al. 2013) produces a faint-end slope that is too steep compared to observations. We find that to match the observed flatter slope, we need a scaling as steep as $\eta \propto \sigma^{-5}$ for $\sigma < 106\,{\rm km\,s^{-1}}$ in our fiducial simulation. All of our simulations adopt $\eta \propto \sigma^{-1}$ at high masses. The need for such a strong scaling at low σ has also been found in the FIRE simulations, which predict an intermediate scaling of $\eta \propto \sigma^{-3.3}$ (M15), as well as in semi-analytic works (Peeples & Shankar 2011; Somerville et al. 2012; Lu et al. 2014) and other cosmological simulations (Pillepich et al. 2018a) that include kinetic feedback. Even though β_η critically affects sub-L_* galaxies at $z = 1$, the different scalings adopted in our test simulations produce similar faint-end slopes of the GSMFs at $z = 0$ and also have little effect on the final masses of massive galaxies. This emphasizes that robust statistical properties of dwarf galaxies at high redshifts are essential to distinguish between different feedback models and to understand how stellar feedback regulates galaxy growth. Such observations will have to await the launch of *JWST*.

Changing the overall strength of outflows by changing the normalization factor α_η also has a clear effect on galaxy growth, with a higher mass-loading factor leading to less star formation, especially in dwarf galaxies at high redshifts (Fig. 4). This dependence of M_* on α_η can be qualitatively explained by a simple analytic model that assumes isolated galaxy growth and negligible wind recycling (Fig. 5).

The evolution of wind particles in a halo is very sensitive to the initial wind speed and the gravitational potential near the centre, which is usually dominated by baryons and is numerically poorly resolved. The winds launched with our new method have wind velocities that agree with the FIRE simulations (M15) at R_{25}, while those launched with the original velocity formula often lose most of their momentum at small radii and even fail to reach R_{25} in massive haloes (Fig. 2). As a consequence, the initial wind speed has a strong impact on the growth of massive galaxies. Contrary to some previous findings that the stellar feedback is only efficient enough to suppress star formation in sub-L_* galaxies, in some of

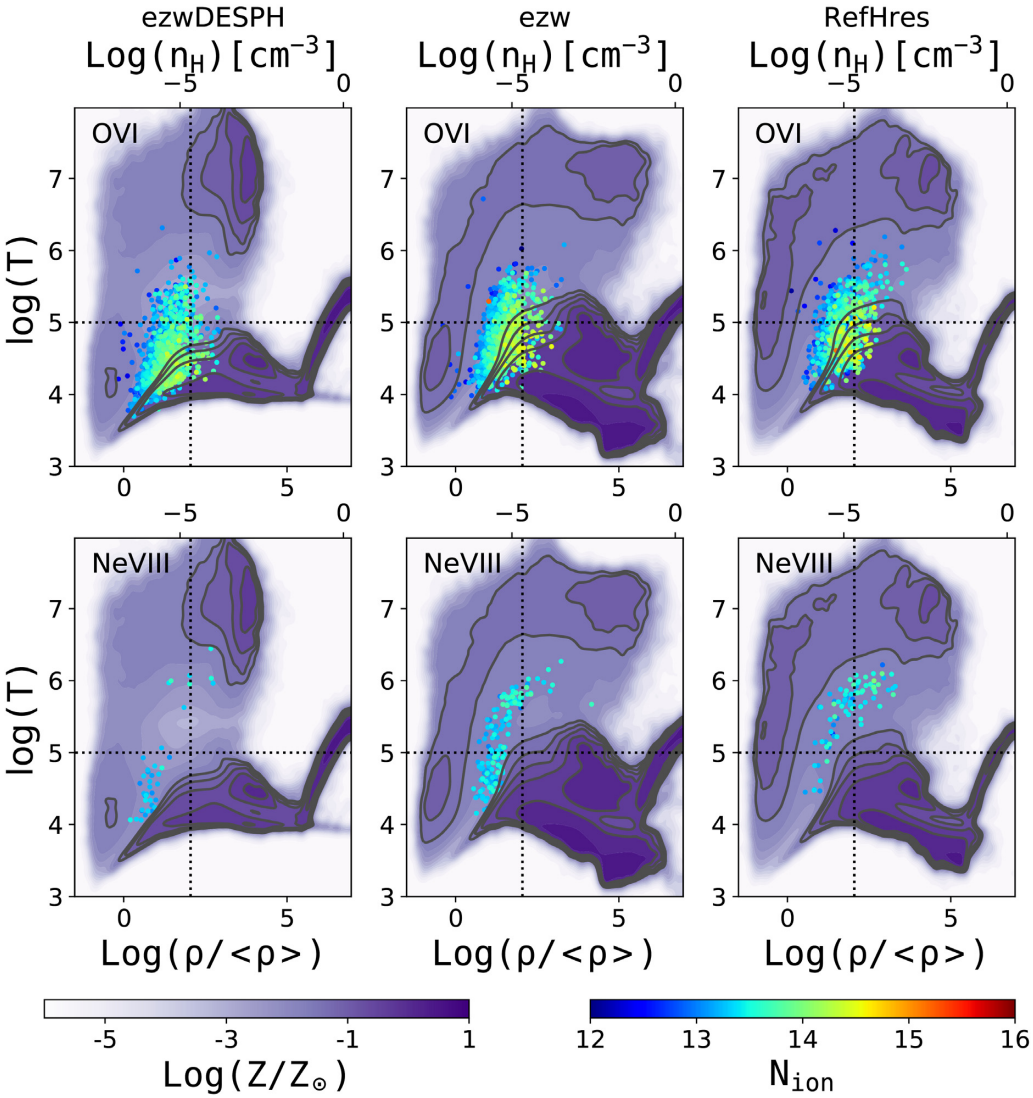

Figure 19. The metal distributions at $z = 0$ in phase space from the ezwDESPH (*left*), ezw (*middle*), and RefHres (*right*) simulations. The purple background colour scale indicates the mass-weighted average metallicity in each cell. In each panel, we show the O VI absorbers or the Ne VIII absorbers on random sightlines that are generated using the technique described in the text. The absorbers are colour coded according to their column densities. The two dotted lines in each panel divide the phase space into four regions: the warm–hot IGM (WHIM, upper left), the diffuse IGM (lower left), hot halo gas (upper right), and cold dense galactic gas (lower right). Several contours lines are stressed for better visualization.

our simulations, including the fiducial simulation, the fast winds do significantly reduce star formation in massive galaxies and bring the massive end of the predicted GSMF at $z = 0$ much closer to observations as long as they are capable of escaping their host galaxies instead of almost instantly falling back as in our original algorithm.

Note, however, that the FIRE simulations only explore haloes as massive as $10^{13}\,M_{\odot}$. Below this mass scale, the FIRE simulations are able to reproduce the stellar mass–halo mass relation without any AGN feedback (Feldmann et al. 2017), supporting our results that stellar feedback alone might be sufficient to suppress star formation up to this mass scale. However, in our wind algorithm, we extrapolate the empirical relation between v_{25} and v_c to even more massive systems by adjusting the initial wind velocities. Therefore, our results at the massive end of the GSMFs should not be interpreted as a consequence derived from physical assumptions but they rather show that the wind speed, as well as how winds propagate and stay in the halo, has strong effects on galaxy evolution.

We further study how the initial wind speed could affect our simulation results by comparing our fiducial simulation with the RefSlow simulation, a simulation with slower wind speeds (Figs 6–8). Changing the wind speed significantly affects star formation in massive galaxies but has little effect in low-mass galaxies. In the most massive galaxies of the two simulations, the average wind speed differs by a factor of ∼2, and the stellar masses differ by ∼0.2–0.4 dex at different redshifts. This leads to clear differences at the massive end of the GSMFs, where the statistical variance is large.

The faster wind speeds in the fiducial simulation relative to our older *ezw* algorithm drive wind particles further from their host galaxy. It also heats more wind particles to the temperature of the hot corona, making them have to cool before re-accreting and hence reducing their re-accretion rate (Figs 9–11). Both effects

lengthen the recycling time of the wind particles and make wind recycling less efficient than simulations with slower wind speeds (Fig. 13). However, wind recycling still dominates accretion on to the massive galaxies at low redshifts, fuelling too much late star formation. Hot accretion is also responsible for 25 per cent of the total mass of stars formed in the massive galaxies at $z = 0$ and also needs to be significantly suppressed to have these galaxy stellar masses match observations. Mergers play only a limited role in the growth of massive galaxies and are nearly negligible for low-mass and intermediate-mass galaxies (Fig. 12). However, if one removes all the late-time star formation in massive galaxies required to match observations, the merger growth could become much more important.

This sensitivity to the initial launch speed also implies that the simulations are sensitive to numerical resolution that affects the accuracy of force calculations near the centre of the haloes and the physical assumptions that govern the propagation of winds in the haloes. We empirically find that in our fiducial simulation RefHres, which has twice the spatial resolution and eight times the mass resolution as the other simulations, we need to enhance the wind speed by an overall factor of $\sim$1.14 to match the constraints at R_{25}. After this correction, the galaxy properties of the fiducial simulation are similar to those of the corresponding lower resolution simulation. It implies that recalibration of the initial wind speed at different resolutions is necessary in subgrid wind implementations that are similar to ours. Instead of matching observational constraints such as the stellar mass functions, it is likely sufficient to tune the parameters to reproduce the same wind speed at a certain radius, after which wind propagation becomes largely independent of resolution. In this work, we choose R_{25} because of the constraints from the FIRE simulations (M15).

With the new wind model and a fiducial set of wind parameters, we run a simulation (RefHres) with higher numerical resolution than these test simulations. This simulation results in GSMFs, SMHMs, and SDEs that are in much better agreement with observations at all redshifts than the original *ezw* wind. However, it still produces too many stars in massive galaxies at $z = 0$. The cold gas fractions agree well with observations and are not significantly affected by the new wind algorithm. The fiducial simulation produces slightly more high column density absorbers for high ions such as O VI and Ne VIII, but this result is sensitive to numerical resolution.

Despite many changes in both numerical algorithms and wind implementations, our new simulations confirm three key conclusions of our previous work: cold accretion produces most of the gas that forms stars in low-mass haloes, hot accretion takes over from cold accretion in high-mass haloes, and wind recycling is an essential component of galaxy growth at redshifts $z < 1$ (Kereš et al. 2005, 2009a, b; Oppenheimer et al. 2010). However, the details of the wind implementation have a large impact on the amount and mass dependence of wind recycling. Reproducing the observed stellar masses in high-mass haloes likely requires an additional mechanism that suppresses hot gas accretion, and AGN feedback is a natural candidate for this mechanism (Benson et al. 2003; Bower et al. 2006; Croton et al. 2006). However, we should be cautious in drawing lessons about AGN feedback scaling because the amount of feedback required is sensitive to still uncertain aspects of galactic winds driven by stellar feedback. In this paper, we have focused on the effects of wind launch algorithms, but our simulations also suffer from underresolving the physics of ejected wind gas after it has entered the CGM. This is probably true of all current cosmological simulations, even zoom-in simulations that attempt to resolve parsec-level structure on the ISM. Forcing high resolution in the CGM is one approach to this problem (Hummels et al. 2019; Peeples et al. 2019; van de Voort et al. 2019), though even so it may be difficult to resolve the relevant scales of instabilities and fluid mixing (Scannapieco & Brüggen 2015; Schneider & Robertson 2017). Another approach is to develop an explicit subgrid model for evolving wind particles after they leave the galaxy, so that wind propagation and recycling, which we have shown to critically affect many simulation results, are controlled by physical parameters instead of unresolved numerics. We will present such a model in future work.

ACKNOWLEDGEMENTS

We acknowledge support by NSF grant AST-1517503, NASA ATP grant 80NSSC18K1016, and *HST* Theory grant HST-AR-14299. DW acknowledges support of NSF grant AST-1909841.

REFERENCES

Agertz O., Kravtsov A. V., Leitner S. N., Gnedin N. Y., 2013, ApJ, 770, 25
Anglés-Alcázar D., Faucher-Giguère C.-A., Kereš D., Hopkins P. F., Quataert E., Murray N., 2017, MNRAS, 470, 4698
Asplund M., Grevesse N., Sauval A. J., Scott P., 2009, ARA&A, 47, 481
Baldry I. K. et al., 2012, MNRAS, 421, 621
Behroozi P. S., Wechsler R. H., Conroy C., 2013, ApJ, 770, 57
Benson A. J., Bower R. G., Frenk C. S., Lacey C. G., Baugh C. M., Cole S., 2003, ApJ, 599, 38
Bernardi M., Meert A., Sheth R. K., Vikram V., Huertas-Company M., Mei S., Shankar F., 2013, MNRAS, 436, 697
Bower R. G., Benson A. J., Malbon R., Helly J. C., Frenk C. S., Baugh C. M., Cole S., Lacey C. G., 2006, MNRAS, 370, 645
Chabrier G., 2003, PASP, 115, 763
Christensen C. R., Davé R., Governato F., Pontzen A., Brooks A., Munshi F., Quinn T., Wadsley J., 2016, ApJ, 824, 57
Conroy C., Gunn J. E., White M., 2009, ApJ, 699, 486
Crain R. A. et al., 2015, MNRAS, 450, 1937
Croton D. J. et al., 2006, MNRAS, 365, 11
Cullen L., Dehnen W., 2010, MNRAS, 408, 669
Dalla Vecchia C., Schaye J., 2008, MNRAS, 387, 1431
Davé R., Hernquist L., Weinberg D. H., Katz N., 1997, ApJ, 477, 21
Davé R., Oppenheimer B. D., Katz N., Kollmeier J. A., Weinberg D. H., 2010, MNRAS, 408, 2051
Davé R., Oppenheimer B. D., Finlator K., 2011a, MNRAS, 415, 11
Davé R., Finlator K., Oppenheimer B. D., 2011b, MNRAS, 416, 1354
Davé R., Katz N., Oppenheimer B. D., Kollmeier J. A., Weinberg D. H., 2013, MNRAS, 434, 2645
Davé R., Thompson R., Hopkins P. F., 2016, MNRAS, 462, 3265
Feldmann R., Quataert E., Hopkins P. F., Faucher-Giguère C.-A., Kereš D., 2017, MNRAS, 470, 1050
Finlator K., Davé R., 2008, MNRAS, 385, 2181
Ford A. B., Oppenheimer B. D., Davé R., Katz N., Kollmeier J. A., Weinberg D. H., 2013, MNRAS, 432, 89
Ford A. B., Davé R., Oppenheimer B. D., Katz N., Kollmeier J. A., Thompson R., Weinberg D. H., 2014, MNRAS, 444, 1260
Ford A. B. et al., 2016, MNRAS, 459, 1745
Furlong M. et al., 2015, MNRAS, 450, 4486
González V., Labbé I., Bouwens R. J., Illingworth G., Franx M., Kriek M., 2011, ApJ, 735, L34
Haardt F., Madau P., 2012, ApJ, 746, 125
Heckman T. M., Borthakur S., 2016, ApJ, 822, 9
Hopkins P. F., 2013, MNRAS, 428, 2840
Hopkins P. F., Quataert E., Murray N., 2012, MNRAS, 421, 3522
Hopkins P. F. et al., 2018, MNRAS, 480, 800
Huang S. et al., 2019, MNRAS, 484, 2021
Hummels C. B. et al., 2019, ApJ, 882, 156
Ilbert O. et al., 2013, A&A, 556, A55

Kereš D., Katz N., Weinberg D. H., Davé R., 2005, MNRAS, 363, 2
Kereš D., Katz N., Fardal M., Davé R., Weinberg D. H., 2009a, MNRAS, 395, 160
Kereš D., Katz N., Davé R., Fardal M., Weinberg D. H., 2009b, MNRAS, 396, 2332
Kewley L. J., Ellison S. L., 2008, ApJ, 681, 1183
Leroy A. K., Walter F., Brinks E., Bigiel F., de Blok W. J. G., Madore B., Thornley M. D., 2008, AJ, 136, 2782
Li C., White S. D. M., 2009, MNRAS, 398, 2177
Lu Y. et al., 2014, ApJ, 795, 123
McGaugh S. S., 2005, ApJ, 632, 859
McGaugh S. S., 2012, AJ, 143, 40
Martin C. L., 2005, ApJ, 621, 227
Mitchell P. D., Lacey C. G., Baugh C. M., Cole S., 2013, MNRAS, 435, 87
Moster B. P., Naab T., White S. D. M., 2018, MNRAS, 477, 1822
Moustakas J. et al., 2013, ApJ, 767, 50
Muratov A. L., Kereš D., Faucher-Giguère C.-A., Hopkins P. F., Quataert E., Murray N., 2015, MNRAS, 454, 2691, (M15)
Murray N., Quataert E., Thompson T. A., 2005, ApJ, 618, 569
Murray N., Quataert E., Thompson T. A., 2010, ApJ, 709, 191
Murray N., Ménard B., Thompson T. A., 2011, ApJ, 735, 66
Muzzin A. et al., 2013, ApJ, 777, 18
Oppenheimer B. D., Davé R., 2006, MNRAS, 373, 1265
Oppenheimer B. D., Davé R., 2008, MNRAS, 387, 577
Oppenheimer B. D., Davé R., Kereš D., Fardal M., Katz N., Kollmeier J. A., Weinberg D. H., 2010, MNRAS, 406, 2325
Oppenheimer B. D., Davé R., Katz N., Kollmeier J. A., Weinberg D. H., 2012, MNRAS, 420, 829
Peeples M. S., Shankar F., 2011, MNRAS, 417, 2962
Peeples M. S., Werk J. K., Tumlinson J., Oppenheimer B. D., Prochaska J. X., Katz N., Weinberg D. H., 2014, ApJ, 786, 54
Peeples M. S. et al., 2019, ApJ, 873, 129
Pillepich A. et al., 2018a, MNRAS, 473, 4077
Pillepich A. et al., 2018b, MNRAS, 475, 648
Popping G. et al., 2015, MNRAS, 454, 2258
Read J. I., Hayfield T., 2012, MNRAS, 422, 3037
Rupke D. S., Veilleux S., Sanders D. B., 2005, ApJS, 160, 115
Sadoun R., Shlosman I., Choi J.-H., Romano-Díaz E., 2016, ApJ, 829, 71
Saintonge A. et al., 2011, MNRAS, 415, 32
Sanders R. L. et al., 2015, ApJ, 799, 138
Scannapieco E., Brüggen M., 2015, ApJ, 805, 158
Scannapieco C. et al., 2012, MNRAS, 423, 1726
Schaye J. et al., 2015, MNRAS, 446, 521
Schneider E. E., Robertson B. E., 2017, ApJ, 834, 144
Sembolini F. et al., 2016a, MNRAS, 457, 4063
Sembolini F. et al., 2016b, MNRAS, 459, 2973
Smit R. et al., 2014, ApJ, 784, 58
Somerville R. S., Gilmore R. C., Primack J. R., Domínguez A., 2012, MNRAS, 423, 1992
Song M. et al., 2016, ApJ, 825, 5
Springel V., 2005, MNRAS, 364, 1105
Springel V., Hernquist L., 2003, MNRAS, 339, 312
Stinson G., Seth A., Katz N., Wadsley J., Governato F., Quinn T., 2006, MNRAS, 373, 1074
Tomczak A. R. et al., 2014, ApJ, 783, 85
Tremonti C. A. et al., 2004, ApJ, 613, 898
Tumlinson J., Peeples M. S., Werk J. K., 2017, ARA&A, 55, 389
Valentini M., Murante G., Borgani S., Monaco P., Bressan A., Beck A. M., 2017, MNRAS, 470, 3167
van de Voort F., Springel V., Mandelker N., van den Bosch F. C., Pakmor R., 2019, MNRAS, 482, L85
Weinberger R. et al., 2016, MNRAS, 465, 3291
Wiersma R. P. C., Schaye J., Smith B. D., 2009, MNRAS, 393, 99
Zhang D., 2018, Galaxies, 6, 114

This paper has been typeset from a TEX/LATEX file prepared by the author.